

The HD(CP)² Observational Prototype Experiment HOPE – An Overview

5 Andreas Macke¹, Patric Seifert¹, Holger Baars¹, Christian Barthlott², Christoph Beekmans³, Andreas Behrendt⁴, Birger Bohn⁵, Matthias Brueck⁶, Johannes Bühl¹, Susanne Crewell⁸, Thomas Damian², Hartwig Deneke¹, Sebastian Düsing¹, Andreas Foth⁹, Paolo Di Girolamo¹⁰, Eva Hammann³, Rieke Heinze^{6,7}, Anne Hirsikko^{5,13}, John Kalisch^{1,11}, Norbert Kalthoff², Stefan Kinne⁶, Martin Kohler², Ulrich Löhnert⁸, Bomidi Lakshmi Madhavan^{1,14}, Vera Maurer^{2,15}, Shravan Kumar Muppa⁴, Jan Schween⁸, Ilya Serikov⁶, Holger Siebert¹, Clemens Simmer³, Florian Späth⁴, Sandra Steinke⁸, Katja Träumner^{2,12}, Silke Trömel³, Birgit Wehner¹, Andreas Wieser², Volker Wulfmeyer⁴, Xinxin Xie³

¹Leibniz Institute for Tropospheric Research (TROPOS), Leipzig, Germany

²Institute of Meteorology and Climate Research - Troposphere Research (IMK-TRO), Karlsruhe Institute of Technology (KIT), Karlsruhe, Germany

15 ³Meteorological Institute, University of Bonn, Bonn, Germany

⁴Institute of Physics and Meteorology (IPM), University of Hohenheim, Stuttgart, Germany

⁵Institute of Energy and Climate Research (IEK-8), Forschungszentrum Jülich GmbH (FZJ), Jülich, Germany

⁶Max-Planck-Institut für Meteorologie (MPIM), Hamburg, Germany

⁷Institut für Meteorologie und Klimatologie, Leibniz Universität Hannover, Hannover, Germany

20 ⁸Institute for Geophysics and Meteorology (IGMK), University of Cologne, Cologne, Germany

⁹Leipzig Institute of Meteorology, University of Leipzig, Leipzig, Germany

¹⁰Scuola di Ingegneria, Università degli Studi della Basilicata, Potenza, Italy

¹¹Department of Energy and Semiconductor Research, Institute of Physics – Oldenburg University, Oldenburg, Germany

¹²NDT Global GmbH & Co. KG, Stutensee, Germany

25 ¹³Finnish Meteorological Institute, Helsinki, Finland

¹⁴Department of Marine Sciences, Goa University, Goa, India

¹⁵German Weather Service (DWD), Offenbach, Germany

Correspondence to: Andreas Macke (andreas.macke@tropos.de)

Abstract. The “HD(CP)² Observational Prototype Experiment” (HOPE) was performed as a major 2-month field experiment in Jülich, Germany, in April and May 2013, followed by a smaller campaign in Melpitz, Germany in September 2013. HOPE has been designed to provide a observational dataset for a critical evaluation of the new German community atmospheric Icosahedral non-hydrostatic (ICON) model at the scale of the model simulations and further to provide information on land-surface-atmospheric boundary layer exchange, cloud and precipitation processes as well as on sub-grid variability and microphysical properties that are subject to parameterizations. HOPE focuses on the onset of clouds and precipitation in the convective atmospheric boundary layer. The paper summarizes the instrument set-ups, the intensive observation periods as well as example results from both campaigns.

HOPE-Jülich instrumentation included a radio sounding station, 4 Doppler lidars, 4 Raman lidars (3 of them provide temperature, 3 of them water vapour and all of them particle backscatter data), 1 water-vapour differential absorption lidar, 3 cloud radars, 5 microwave radiometers, 3 rain radars, 6 sky imagers, 99 pyranometers, and 5 Sun photometers operated at

different sites, some of them in synergy. The HOPE-Melpitz campaign combined ground-based remote sensing of aerosols and clouds with helicopter- and balloon-based in-situ observations in the atmospheric column and at the surface.

HOPE provided an unprecedented collection of atmospheric dynamical, thermodynamical, and micro- and macrophysical properties of aerosols, clouds and precipitation with high spatial and temporal resolution within a cube of approximately 10 x 10 x 10 km³. HOPE data will significantly contribute to our understanding of boundary layer dynamics and the formation of clouds and precipitation. The datasets have been made available through a dedicated data portal.

First applications of HOPE data for model evaluation have shown a general agreement between observed and modelled boundary layer height, turbulence characteristics, and cloud coverage, but also point to significant differences that deserve further investigations, both from the observational and from the modelling perspective.

10 **1 Introduction**

Clouds and precipitation play a central role in the climate system and were repeatedly identified as the largest problem in a realistic modelling of atmospheric processes, forcings and feedbacks (IPCC, 2013; Jakob, 2010). Uncertainties in the characterization of clouds and precipitation have manifold consequences on virtually all non-atmospheric climate components from ocean mixed layer stability to vegetation variability, to net mass balance of ice sheets (Wilson and Jetz, 2016).

15 To achieve progress in the improvement of the representation of clouds and precipitation in atmospheric models, the German research initiative "High Definition Clouds and Precipitation for advancing Climate Prediction" HD(CP)² was launched. HD(CP)² aims at a significant reduction in the uncertainty of climate change predictions by means of better resolving cloud and precipitation processes. The newly developed convection-resolving HD(CP)² Icosahedral non-hydrostatic model (ICON) will be used to develop new convection parameterizations for future application in large-scale general circulation models (GCM) and climate models. HD(CP)² and the accompanied development of ICON originated from a coordinated initiative of
20 German research institutions, the German Meteorological Service (DWD), and the Federal Ministry of Education and Research to provide atmospheric scenarios, including multiple thermodynamic phases, multi-mode microphysics, and a realistic orography with high spatial resolution of 100 m in the horizontal and 10 - 50 m in the vertical at a temporal resolution of 1-10 s over climatologically relevant scales, i.e. over several thousand kilometres and several years. The 100-m scale is believed to
25 be most critical for the onset of clouds and precipitation as it sufficiently resolves the convective boundary layer and cloud formation (Stevens and Lenschow, 2001). The anticipated high resolution shall thus enable to associate differences in modelled and observed atmospheric fields to problems with the dynamical core or with parameterizations of physical processes rather than with resolution issues.

The HD(CP)² project consists of a modelling, an observational, and a synthesis part (see <http://www.hdep2.eu> for further
30 information concerning the overall project descriptions and goals). As a first step of HD(CP)², the high-resolution HD(CP)² model in LES mode must be evaluated in order to test the suitability for parameterization development application. The test bed for these observations was provided by means of the "HD(CP)² Observational Prototype Experiment" HOPE.

Within the M-module (modelling) of HD(CP)², the new ICON general circulation model was developed (Zängl et al., 2015) and its performance in LES modelling was evaluated (Dipankar et al., 2015). The O-module (Observations) was defined to provide observational datasets for the initialization and evaluation of the newly developed ICON model and other high-resolved LES models as well as for the development of new parameterizations that are suitable for application in a high-resolution model. The scope of the S-module (synthesis) was to provide first improvements of parameterizations from the use of model and observation results. Key to this effort was the provision of modelled scenarios at 100-m grid resolution over thousands of kilometres, which will be used to analyse, improve or develop parameterizations related to cloud and precipitation development in climate models.

The O4 project in the O module of HD(CP)² was devoted to HOPE and has been designed to provide a critical model evaluation at the scale of the model simulations and further to provide information on sub-grid variability and microphysical properties that are subject to parameterizations even at high-resolution simulations such as planned with ICON. Even for LES, unresolved sub-grid scale processes are believed to be in particular critical for cloud formation and the onset of precipitation, and thus built the central focus of HOPE. In order to derive the atmospheric state and the 3D fields of water vapour, temperature, wind and cloud and precipitation properties at the scale of 100-m resolution for an area of about 10x10x10 km³ three close-by supersites, separated by a distance of approximately 4 km, complemented by larger networks were deployed. The instrumentation was selected in order to allow for detailed observations of the onset of clouds and precipitation in the convective atmospheric boundary layer. When compared to model results, the high-resolution HOPE data could elucidate to what extent a pure increase in model resolution improves model skills in the atmospheric boundary layer, and to what extent unavoidable parameterizations of physical processes - essentially turbulence and cloud microphysics - require new approaches. HOPE complements the larger spatiotemporal Full-Domain (O2) and Supersites (O1) activities in the observations module in HD(CP)² of which O2 provides continuous time series of 2D fields across the HD(CP)² domain and O1 is devoted to the provision of 1D profiles at four dedicated locations in Germany and the Netherlands, respectively. The scope of Module O3 was to establish a data flow from the observation modules to the model and synthesis modules. In 2016, HD(CP)² entered its second phase, which puts a much stronger effort on the synthesis part. HOPE builds on the experience gained in previous field campaigns like the Convective and Orographically-induced Precipitation Study (COPS) (Wulfmeyer et al., 2011), however, with a stronger focus on multi-sensor synergy covering a micro- to meso-scale domain. COPS and the associated General Observation Period (GOP) that was prepared in the context of the Quantitative Precipitation Forecasting priority program (SPP1167) of the German Science Foundation (DFG) (Crewell et al., 2008) aimed at the observation of orographically driven initiation of convection with supersites several tens of km apart in strongly structured terrain. Complementary to COPS, HOPE is covering a smaller domain with higher resolution, and is accompanied by long-term supersite observations within the framework of the Terrestrial Environmental Observatoria (TERENO) Programme (Simmer et al., 2015) around the ground-based remote sensing supersite JOYCE (Löhnert et al., 2015), and the TROPOS long-term aerosol observatory in Melpitz (Spindler et al., 2012).

Although phase 1 of HD(CP)², lasting from 2012 to 2015, was mainly devoted to establish a scalable high-resolution ICON model and to obtain data for model evaluation at various scales, first highly resolved ICON-based LES have been performed to evaluate the effect of resolution on reproducing boundary layer fluxes and heights, as well as on cloud formation. First results are reported in this overview.

5 This article mainly serves as a guide through the sites and instrumentation used during the HOPE campaigns and it is aiming on giving a motivation to learn about the details and specific conclusions described in the individual publications this overview is built upon. The structure is as follows. Section 2 describes the site setups and measurements performed during HOPE including information about the meteorological conditions and data availability. Examples from each of the research topics are presented in section 3. In section 4, first comparisons between models and observations are discussed. A summary and
10 conclusions on the further applications of the HOPE data as well as designs for future observational strategies are presented in section 5. Individual work performed during HOPE is published in this ACP/AMT HOPE special issue or, in part, in other journals and is cited in the present overview correspondingly.

2 Description of the HOPE field campaigns

The technological aspect of HOPE was to unite most of the mobile ground-based remote sensing and surface flux observations
15 available in Germany within a single domain in order to capture the vertical structure and horizontal variability of wind, temperature, humidity as well as aerosol and cloud condensate with the best possible temporal and spatial resolution. Thus we were able to accommodate active remote sensing from lidar and radar, and passive remote sensing from microwave radiometer and Sun photometer, whenever possible with scanning capabilities. During HOPE, 3D water-vapour, temperature, and wind
20 measurements were possible with unprecedented spatiotemporal resolution in the boundary layer. In order to understand the forcing of and the response to surface properties, distributed surface flux and surface standard meteorological observations were deployed as well. Of course, it is not possible to obtain an instantaneous 3D picture of the atmosphere from a limited number of directional observations. However, ongoing improvements in sensor detection accuracy and optimized scanning strategies will capture the 4D boundary layer properties even better in the future.

The measurement activities during HOPE mainly consisted of a major field experiment in Jülich, Germany, denoted as HOPE-
25 Jülich, conducted from April 3 to May 30, 2013 followed by a smaller campaign that was performed in Melpitz, denoted as HOPE-Melpitz, Germany, which was conducted from September 9 to September 29, 2013. Figures 1 and 2 give an overview of the broad spectrum of instruments installed during the two campaigns and their overall setup. A detailed introduction is given below.

2.1 Instrumentation

2.1.1 HOPE-Jülich

In order to derive the atmospheric state of water vapor, temperature, wind and cloud and precipitation properties with 100-m resolution for an area of about 10x10x10 km³ three close-by (ca. 4 km) supersites, complemented by larger networks, were operating. Figure 3 gives an overview about the different sites and networks within HOPE-Jülich, which are further described in Table 1. The monitored area encompasses approximately 40 km in radius around the Research Centre of Jülich. The natural topography around Jülich is rather flat with an average elevation of around 100 m above sea level (asl). Approximately 20 km south of Jülich the Eifel Mountains approach up to 800 m asl. Locally, within a radius of 10 km, the area around Jülich is dominated by open pit coal mining. Two open pit mines are located within 1-3 km east and west of the HOPE-Jülich area, respectively. Along a 10-km line between these two pit mines, the elevation range spans over 571 m, from as low as -270 m asl within the pit mines (pit mine of Hambach, see Figure 3) to 301 m asl at the top of the debris hill Sophienhöhe. The instruments and observations were deployed at supersites in the rather flat terrain between the pit mines or within networks. The TERENO sites as well as the X-band radar sites JuXPol and BoXPol that are shown in Figure 3 also contributed to the HOPE observations, even though they are operated in the frame of other research projects, mainly Terrestrial Environmental Observatories (TERENO) (Zacharias et al., 2011) and the Transregional Collaborative Research Centre 32 (TR32) (Simmer et al., 2015), which are implemented for longer time periods than was the case for HOPE.

As can be seen from Table 1, most instruments were deployed at the three supersites Jülich (JUE), Krauthausen (KRA), and Hambach (HAM) with its outpost close to a pump station “Wasserwerk” (WAS). At each supersite one or several main remote-sensing facilities were deployed. At JUE this was the instrumentation of the permanently installed Jülich Observatory for Cloud Evolution (JOYCE), at HAM the Karlsruhe Institute for Technology mobile facility KITcube and the lidar systems of the Institute for Physics and Meteorology (IPM) of the University of Hohenheim (UHOH) were deployed, and at KRA the Leipzig Aerosol and Cloud Remote Observations System (LACROS) was operated. In some publications that are based on HOPE-Jülich observations, the supersite names are also referring to the main facility deployed at each site, e.g. LAC for LACROS at the supersite KRA, JOY for JOYCE at the supersite JUE, and KIT for KITcube at the supersite HAM. The instrumentation that was present at each site is listed in Table 2. In total, the HOPE-Jülich set of instruments included a radio sounding station, 5 Doppler lidars, 4 Raman lidars, 1 differential absorption lidar (DIAL), 3 cloud radars, 5 microwave radiometers (MWR), 3 precipitation radars, 6 sky imagers, 99 pyranometers, and 5 Sun photometers. Below, the operating institutions and available measurement devices at all three supersites are briefly outlined. Concerning technical details of the individual instruments, such as instrument calibration and stability, restrictions in the instrument resolution, or the assessment of uncertainties, we refer the reader to the literature cited in Table 2. In addition, results shown in Sect. 3 and 4 of this article are based on already published articles which are cited at the respective positions in text and contain detailed information on the applied instrumentation and methodologies.

Jülich supersite - JUE

All measurements during HOPE-Jülich were built around the central supersite Jülich where JOYCE (Löhnert et al., 2015) is operated continuously at the Research Center Jülich. JOYCE (<http://www.joyce.cloud>) is a joint research initiative of the Institute for Geophysics and Meteorology (IGMK) of the University of Cologne and the Jülich Research Centre (FZJ). It is permanently installed at FZJ. Amongst other instruments (see Löhnert et al. (2015)), JOYCE contributed to HOPE with observations of a continuously scanning 35-GHz cloud radar, a Doppler lidar, and three microwave radiometers (one continuously scanning, one vertically pointing, and one continuously obtaining temperature profiles) for the spatiotemporal characterisation of humidity and liquid water fields and for provision of the line-of-sight-integrated amount of water vapour and liquid water (Rose et al., 2005). The observations at the supersite Jülich were supported by high-resolved measurements of the vertical profile of the atmospheric temperature and water vapour mixing ratio, both at daytime and at night, which have been performed with the multi-wavelength polarization Raman lidar system BASIL of the Università degli Studi della Basilicata (UniBas), Italy (Di Girolamo et al., 2009) and the lidar system ARL-2 of the Max Planck Institute for Meteorology (MPIM) (Wandinger et al., 2016). Temperature and moisture turbulent fluctuations have been observed by BASIL and are reported by Di Girolamo et al. (2016). BASIL as well as the ARL-2 lidar also provided measurements of aerosol scattering properties at 355, 532, and 1064 nm.

Hambach supersite - HAM

With the newly designed observing system KITcube (Kalthoff et al., 2013), the Institute of Meteorology and Climate Research (IMK) of the Karlsruhe Institute of Technology (KIT) provides meteorological and convection-related parameters and contributed to measurements of the development of clouds with high temporal and spatial resolution in the HOPE area. KITcube was the main facility at the supersite Hambach (HAM) and consists of a surface-based network with meteorological stations and a 30-m tower measuring the standard parameters of temperature, humidity, air pressure, wind speed and direction, sensible heat fluxes, the energy balance components at the Earth's surface (Kalthoff et al., 2006) as well as soil moisture and soil temperature profiles (Krauss et al., 2010). These stations in general are distributed over the whole area of KITcube to account for surface inhomogeneity. For instance, KIT operated two Eddy-Covariance stations – one at the main site HAM, and a second one at the outpost WAS, approximately 2.5 km to the west. KITcube also includes scanning Doppler wind lidars to measure wind speed, wind direction, and turbulence characteristics in the convective boundary layer. One Lockheed WindTracer was installed at supersite HAM, a second WindTracer at the outpost WAS (see Fig 3b) to allow Dual-Doppler applications. Both were installed together with a Leosphere Windcube. Additionally, a Doppler lidar of KIT IMK-IFU (Halo Photonics Streamline) was operated at the TERENO site Selhausen. These instruments were complemented by a microwave radiometer, a scanning 35-GHz cloud radar monitoring the development of clouds, a vertically pointing micro rain radar and disdrometers providing information about precipitation, and a ceilometer for cloud base height detection. At a second KITcube outpost denoted KiXPol, approximately 7.5 km southwest of HAM, a polarimetric X-band rain radar was operated, providing volume scans of polarimetric moments, vertical cross-sections (RHI-scans) on demand, as well as the horizontal precipitation

field for the HOPE-Jülich area every 5 minutes and with 250-m radial resolution. In-situ vertical profiles of temperature, humidity, and wind profiles as well as convective indices were gathered by radiosondes launched regularly every 6th full hour at the KITcube main site. Land and full-sky images were taken by S14 camera systems at HAM and WAS.

Also at supersite HAM, two lidar systems from the Institute for Physics and Meteorology (IPM) of the University of Hohenheim observed 3D thermodynamic fields of temperature and moisture including their turbulent fluctuations. A temperature rotational Raman lidar (TRRL) measured temperature profiles (Radlach et al., 2008; Hammann et al., 2015) and a water-vapour differential absorption lidar (DIAL) measured absolute humidity profiles (Behrendt et al.; Späth et al., 2016; Wagner et al., 2013). In contrast to the Raman lidar technique, the DIAL technique, which is based on the alternating emission of laser pulses at frequencies strongly and weakly absorbed by water vapour, does not require calibration. By sending out the laser beam vertically into the atmosphere, high-resolution observations of the convective boundary layer and the lower free troposphere can be made with the instrument (Muppa et al., 2016; Wagner et al., 2013). But the same system also allows for observations in any direction of interest and thus to map the structure of the water vapour field and its development (Milovac et al., 2016). Like the DIAL also the TRRL of IPM has scanning capabilities and an intrinsic high spatial and temporal resolution of 1-10 s and 15-100 m up to a range of about 5 km. Consequently, both systems are capable of resolving turbulent fluctuations in the convective boundary layer from the surface to the entrainment zone. Derived products include statistical moments of moisture and temperature turbulent fluctuations (Behrendt et al., 2015; Muppa et al., 2016; Wulfmeyer et al., 2015), profiles of stability variables such as buoyancy (Behrendt et al., 2011), and the boundary layer depth, aerosol backscatter fields and cloud boundaries. The self-calibrating DIAL technique has excellent absolute accuracy (Bhawar et al., 2011) and has been acknowledged as water-vapour reference standard of WMO.

20

Krauthausen supersite - KRA

Continuous observations with the TROPOS mobile facility LACROS (Leipzig Aerosol and Cloud Remote Observations System) (Bühl et al., 2013) were performed at the supersite KRA. LACROS employs a 35-GHz cloud radar, a multi-wavelength Raman polarization lidar, a ceilometer, a Doppler lidar, a microwave radiometer, an optical disdrometer, as well as an all-sky imager. The Raman polarization lidar Polly^{XT} (Engelmann et al., 2016), deployed at supersite KRA, is part of the lidar network PollyNet (Baars et al., 2016) and provides automatically derived profiles of aerosol scattering properties and water vapour mixing ratio. Observations of the vertical velocity in the boundary layer and at cloud bases were provided by the Doppler Wind lidar WiLi (Bühl et al., 2012). The focus of the LACROS observations was set on the continuous vertical profiling of the full tropospheric column to derive aerosol and cloud microphysical properties and cloud droplet dynamics (Bühl et al., 2016). LACROS at supersite KRA as well as JOYCE at supersite JUE are part of Cloudnet (Illingworth et al., 2007), providing a target categorization mask and microphysical parameters of clouds based on co-located vertically pointing observations of at least a cloud radar, a lidar and a microwave radiometer.

30

Networks deployed in the HOPE-Jülich area

Beside the supersite observations at JUE, KRA, and HAM, also different instrument networks were distributed in the vicinity of the three supersites. The PYR network of 99 autonomous meteorological stations including pyranometers developed by TROPOS (Madhavan et al., 2016b) was deployed within a radius of about 5 km around the supersite JUE to capture the broadband downwelling solar irradiance with high spatial and temporal resolution.

5 The Meteorological Institute of the University of Bonn (MIUB) coordinated the operation of 6 sky imagers within the SKY network that were provided by several partner institutes to obtain imagery for cloud classification and the determination of cloud morphology (Beekmans et al., 2016).

10 Three scanning polarimetric X-band rain radars jointly operated within the XRD network by the University of Bonn (BoXPol), the Jülich Research Centre (JuXPol) (Diederich et al., 2015), and KIT (KiXPol) provided 3D fields of polarimetric moments over the domain and precipitation estimates (Trömel and Simmer, 2012; Xie et al., 2016).

Within the Sun photometer network (SUN), the vertically integrated aerosol characteristics and water vapour field at the three HOPE-Jülich supersites as well as at two more-remote sites (Aachen and Insel Hombroich, see Table 1) were derived. Except for the one operated within JOYCE at supersite JUE, all Sun photometers were provided by NASA Goddard Space Flight Center (GSFC), Langley, USA, and operated by MPIM.

15 Additionally, two ground-based scanning spectral radiometers SpecMACS, from the Munich Institute for Meteorology (MIM) of the Ludwig-Maximilians Universität Munich (Ewald et al., 2015), and EAGLE from Leipzig Institute of Meteorology (LIM) of the University of Leipzig (Jäkel et al., 2013) participated in the campaign. These instruments provide the solar radiation reflected at cloud sides from which vertical profiles of cloud microphysical properties shall be inferred.

20 **2.1.2 HOPE-Melpitz**

The HOPE-Melpitz campaign basically combined the remote sensing of aerosol and cloud properties of the LACROS supersite with the in-situ observations of the helicopter-borne Airborne Cloud Turbulence Observation System ACTOS (Siebert et al., 2013) (see Figure 2). The follow-up campaign HOPE-Melpitz became necessary because of problems with the availability of a helicopter carrying ACTOS during HOPE-Jülich.

25

The Melpitz site (51.525° N, 12.928° E, 86 m asl) is the TROPOS research station for the continuous physical and chemical in-situ aerosol characterization of background aerosol characteristics in central Germany (Spindler et al., 2012). The site is located in a rural area, 40 km northeast of Leipzig (Figure 4). The topography around the Melpitz site is rather flat over an area of several hundred square kilometres, ranging between 100 m asl and 250 m asl. Melpitz is part of the European
30 Monitoring and Evaluation Programme (EMEP) (Tørseth et al., 2012) as well as of the European Aerosols, Clouds and Trace gases Research Infrastructure (ACTRIS) and provides a comprehensive set of in-situ observed chemical, microphysical and optical aerosol properties. Based on the co-location of the ground-based aerosol instrumentation, the airborne ACTOS

platform, and the remote-sensing facility LACROS, the HOPE-Melpitz campaign thus provides the opportunity to investigate the relationship between tropospheric aerosols and clouds and aerosol conditions.

Similar to HOPE-Jülich, during HOPE-Melpitz the LACROS instrumentation comprised the polarization Raman lidar Polly^{XT}-OCEANET (Engelmann et al., 2016) with near-range capabilities, a Humidity-Temperature Profiler (HATPRO) microwave radiometer, the Doppler Wind lidar WiLi, 50 pyranometers, an all-sky imager, and a radiosonde station (provided from KITcube, see Table 2). Two Sun photometers were installed, one at the site of Melpitz and one at TROPOS in Leipzig (51.3° N, 12.4° E, 120 m asl) in order to distinguish rural and urban aerosol conditions.

Measurements of the broadband irradiances at the surface were carried out with a mobile station following the recommendations of the Baseline Surface Radiation Network (McArthur, 2005), and can serve as high-quality reference for the pyranometer network. In addition, spectral irradiances were observed with a rotating shadowband radiometer of type GUVis-3511 (Witthuhn et al., 2016).

Detailed information on the ACTOS setup are given in Siebert et al. (2013). ACTOS provides dynamic, thermodynamic as well as cloud and aerosol microphysical properties of warm shallow boundary layer clouds. The standard ACTOS instrumentation comprises sensors for the wind vector, temperature, and humidity under clear and cloudy conditions. Observed microphysical parameters of liquid clouds include the cloud droplet number-size distribution in the range from 1 to 180 μm as well as the integral properties of this cloud droplet spectrum, e.g., liquid water content and effective radius. Aerosol number-size distributions for the size range from 8 nm to 2.8 μm are obtained with a resolution of 2 minutes. The total aerosol number concentration was recorded in the aerosol particle size range from 8 nm to 2 μm with 1 Hz resolution (Düsing et al., 2017) and with 50 Hz resolution (Wehner et al., 2011). Additionally, a mini-CCNC (Cloud Condensation Nuclei Counter) was used for measuring the CCN number concentration at different supersaturations.

The two ground-based spectral radiometers EAGLE and SpecMACS from LIM and LMU, respectively, that were operated during HOPE-Jülich, were also deployed during HOPE-Melpitz. Besides ACTOS, airborne observations with spectral radiometers for cloud remote sensing from the Freie Universität Berlin (Schröder et al., 2004) were performed on some days.

2.2. Datasets

2.2.2 HOPE-Jülich

HOPE-Jülich was conducted from 3 April to 31 May 2013 as this period in the year favours low-level cloud formation. Only the measurements of the pyranometer network PYR continued until end of July to capture high-Sun conditions. An extensive operation plan, documenting the daily availability of all central instruments of HOPE-Jülich can be found in the supplementary material to this article.

The weather conditions during the campaign varied from several warm and cold front passages interrupted by a few high pressure systems with high-level cirrus clouds at the beginning of the campaign and more low-level convective clouds later on. Since the campaign focused on the onset of clouds and precipitation, IOPs have been called out whenever clear skies,

boundary layer clouds, or precipitation-developing clouds were forecast. During IOPs, instruments requiring continuous human control were measuring in addition to autonomously operating instruments. Furthermore, radiosondes were launched more frequently at supersite Hambach, depending on the weather situation and its variability. Table 3 summarizes the IOPs during HOPE-Jülich and the corresponding weather conditions. IOPs with especially well suited weather conditions have been labelled as "Golden Days" and have been more deeply analysed by all participating groups.

As an example, a detailed depiction of IOP7 (25 April 2013) consisting of a turbulently driven boundary layer development topped with afternoon single cumulus clouds in the afternoon can be found in Löhnert et al. (2015). There, it is demonstrated that a holistic view of the daily development of the boundary layer is only possible through the synergetic treatment of different ground-based remote sensors.

2.2.2 HOPE-Melpitz

Weather conditions have not been optimal for the helicopter operations due to problems with low-level overcast clouds (no flight permit inside clouds) and icing conditions. During the three weeks of the campaign, five IOPs have been performed on which 10 ACTOS flights were performed, covering 15 hours of measurements (Table 4). However, the helicopter flights captured a spectrum of different meteorological conditions as can be seen from Table 4.

2.2.3 Data availability

All officially participating partners have been submitting their quality-controlled data and in a common format to the HD(CP)² Data Archive Center for Standardized Atmospheric Measurement Data (SAMD). Data processing of specific sensors (i.e. microwave radiometer, cloud radar, ceilometer) deployed by different supersites was made uniform. All the data processing is documented by means of metadata. See Stamnas et al. (2016) for a detailed overview on the data format and data base. All data is publicly available since January 2017 (<https://icdc.cen.uni-hamburg.de/index.php?id=samd>).

3 Results

3.1 Near-surface wind field and energy budget

One central goal of HOPE was the characterization of the turbulent structure of the atmospheric boundary layer (ABL). To capture this feature, both, the surface energy budget components and the wind fields near the surface and in the lower boundary layer are required. The set of instruments available during HOPE-Jülich provided a unique opportunity to compare and to correlate vertical-velocity variances from different locations. Maurer et al. (2016) made use of a triangular set-up of three KITcube Doppler lidar systems deployed approximately 3 km apart from each other. This distance was assumed to be sufficient to ensure that the lidars do not monitor the same convective cells at the same time. Nevertheless, they found persistent similar statistical properties of velocity variances measured along the wind direction in contrast to measurements across the wind

direction. This indicates that local organized structures of turbulence can dominate turbulence characteristics and that single turbulence measurements may not be representative for a larger domain.

In a similar approach Träumner et al. (2015) investigated correlation patterns of near-surface wind fields from a Dual Doppler lidar set-up scanning at low elevation angles together with available in-situ wind vectors from ground-based stations. As a
5 measure for anisotropy, integral length scales were defined for the along-stream and the cross-stream wind components. Integral scales provide a measure of the spatial or temporal dimension of turbulent eddies (Wyngaard, 2004). The authors confirmed previous findings of streak-like structures elongated and aligned in the wind direction. Also periodic behaviour in the horizontal wind fields has been identified occasionally. Interestingly, the mean structural pattern could be related to the background wind speed and the atmospheric stability. Still, individual wind fields can vary strongly for the same external
10 forcing. Thus, a characterization of coherence pattern in the otherwise turbulent boundary layer requires extensive spatiotemporal averaging.

Eder et al. (2015) investigated the complete surface energy budget and tested the hypothesis whether so-called turbulent organized structures (TOS), low-frequency structures that fill the entire atmospheric boundary layer, are a major cause for the frequent unclosed surface energy balances as they contribute to the vertical energy fluxes. In fact, by means of data from
15 horizontally and vertically scanning Doppler lidars the authors could show that TOS with time scales larger than 30 minutes extend deep into the surface layer. This finding implies that future turbulent energy exchange studies require the full 3D field of humidity, temperature and velocity in high spatio-temporal resolution, which was also pointed out and elaborated in Wulfmeyer et al. (2016).

Based on the autonomous pyranometer network described in Madhavan et al. (2016b), the representativeness of a single station
20 measurement for spatially extended domains with different area sizes has been investigated. This is an important aspect for the evaluation of model results with observations, where point measurements are mostly compared to grid-box means, and are thus implicitly assumed to have similar statistical properties. Spatial and temporal smoothing have been quantified which limit the representativeness of a point measurement for its surrounding domain size and period. Spatial averaging acts as a low-pass filter and reduces or even completely removes high-frequency spatiotemporal variations. This is illustrated in Figure 5(a),
25 which shows a wavelet-based power spectrum obtained from 99 pyranometer stations, and corresponding estimates of the power spectra for three areas ranging from 1x1 km² to 10x10 km² in size under broken-cloud conditions. Figure 5(b) shows the explained variance (square of Pearson correlation coefficient) of temporal fluctuations of a point measurement and a spatial domain as a function of frequency. It demonstrates the second effect, which describes that the correlation of temporal fluctuations decreases with increasing frequency. The combination of both effects adds up to the total deviation of a point
30 measurement from the spatial mean of an extended domain, which is presented in Figure 5(c). The magnitude of this deviation depends on the domain size, the averaging period, and the synoptic conditions. Broken clouds cause the largest deviations in the 10x10 km²-sized domain, reaching about 30 W m⁻² for 3-hourly and 80 W m⁻² for 1-s-resolution observations.

Also based on the horizontally high resolved measurements of the irradiance from the pyranometer network (PYR) performed by TROPOS, Lohmann et al. (2016) analysed the statistics of spatiotemporal irradiance fluctuations with a strong application-

oriented focus on photovoltaic power systems. They specifically calculated single-point statistics and two-point correlation coefficients for clear, overcast and mixed skies. The statistics for clear and overcast skies show similar behavior as in previously published work, see Lohmann et al. (2016) for references. In order to account for conditions for a distributed PV system, they defined so-called irradiance increments as changes in transmissivities over specified intervals of time, and showed
5 that the magnitude of increments is more strongly reduced by spatial averaging than that of the fluctuations. By conditioning the sky type - which can easily be done from the irradiance measurements themselves - they demonstrated that the probability for strong irradiance increments is twice as high compared to increment statistics computed without distinguishing between different sky types.

As clouds impose the largest short-term variability in solar irradiance at the surface the analysis of cloud advection and
10 subsequent extrapolation represents a reasonable approach for short-term irradiance forecasts. Schmidt et al. (2016) made use of time series of hemispheric sky images to predict the surface irradiance by means of mapping the cloud position, which in turn is translated into shadow maps at the surface. The temporal evolution of such shadow maps is calculated from cloud motion vectors that were calculated from subsequent sky images. Irradiance forecasts of up to 25 minutes have been produced and were validated against the network of pyranometers described in Madhavan et al. (2016b). Although these sky-imager-
15 based forecasts do not outperform a simple persistence forecast on average, improved forecast skill was found for convective cloud conditions with high cloud and irradiance variability. This finding may provide useful application in photovoltaic electricity production.

3.2 The turbulence structure of the boundary layer and clouds

20 The goal of the HD(CP)² project was to realize and to evaluate a model run spanning the area of whole Germany at the horizontal resolution of 100 m. At such a small scale, certain parameterizations for organized turbulent motions such as those that define the atmospheric boundary layer, and areas of shallow convection are supposed to be not required anymore. Hence, the setup of the envisioned model is comparable to the one of a large-eddy-simulation (LES), wherein the sub-grid parameterizations are simpler and have less impact on the model performance (Bryan et al., 2003;Deardorff, 1970).

25 The increased model resolution puts new requirements on evaluation techniques. The HOPE experiments provided an optimum test bed for novel applications to derive boundary layer fluxes and turbulence characteristics. Observations of the turbulent fluxes of thermodynamic properties in the PBL, such as of temperature and water vapour, provide detailed information on the minimum resolution required by a model to capture the turbulence spectrum down to the inertial sub-range and consequently to resolve the major part of the turbulent fluctuations. This value is in here introduced as the integral scale. During HOPE-
30 Jülich, it was possible to derive based on lidar observations the statistics of turbulent temperature fluctuations and thus of the integral scale of this parameter in the PBL (Behrendt et al., 2015). In addition to commercially available Doppler lidar systems, which provide turbulent wind fluctuations, three water vapour research lidars were deployed during HOPE-Jülich, which provide turbulent humidity fluctuations that were documented by Di Girolamo et al. (2016), as well as Muppa et al. (2016).

As the authors of the above-mentioned studies note, HOPE-Jülich provided for the first time data to observe the turbulence characteristics of the PBL, more specifically the convective boundary layer (CBL), up to the fourth statistical moment, i.e., the mean, standard deviation, variance, skewness, and kurtosis of the spatiotemporal water vapour and temperature. Examples of the relationship between the integral scales (introduced in section 3.1) of humidity and temperature fluctuation and height above ground within the CBL for the 20 April 2013 (IOP 5), 11:30-13:30 UTC, (only temperature fluctuations; see Di Girolamo et al. (2016)) and 24 April 2013 (IOP 6), 11:00-12:00 UTC (temperature and humidity fluctuation; see Behrendt et al. (2015) and Muppa et al. (2016)), respectively, are depicted in Figure 6. A decrease in the integral length scale of the water vapour mixing ratio with height in the upper part of the CBL was found at the HAM site similar to previous observations (Couvreur et al., 2005; Wulfmeyer et al., 2010). A similar decrease was found for temperature at the same site. The temperature observations from JUE site show a more complex structure. The reasons for this are still under investigation. The decrease of the integral length scale toward the top of the CBL can be explained by the decrease in the size of the turbulent eddies with height resulting from the entrainment of dry free-tropospheric air at the CBL top (Couvreur et al., 2005) which is also characterized by an increase in the variance of the temperature or water vapour toward CBL top. Converting the observed time scales shown in Figure 6 to spatial scales assuming horizontal and vertical wind velocities of 5 m s^{-1} and 1 m s^{-1} , respectively, results in horizontal and vertical integral length scales of 100-1000 m and 20-200 m, respectively. Thus, in order to capture the full turbulence spectrum in the CBL, a numerical model simulation should also be run at temporal and spatial resolutions that are better resolved than the observed values.

Detailed convective boundary layer turbulence characteristics from HOPE and further field campaigns (Wulfmeyer et al., 2016) showed that the combination of active temperature-, humidity- and wind-profiling applied during HOPE-Jülich sufficiently resolves the turbulence structure of the CBL and lays the groundwork for new boundary layer turbulence parameterizations.

In addition to turbulent fluxes in the cloud-free planetary boundary layer, the turbulence characteristics of a stratocumulus layer were investigated simultaneously with ACTOS and the Doppler lidar WiLi of the LACROS site on 22 September 2013 during HOPE Melpitz. The inter-comparison shown in Figure 7 presents a histogram of the vertical velocities observed with ACTOS (red) and WiLi (blue), further insights into the microphysical properties of the cloud layer are given in Sec. 3.4 and Figure 12. The variability of the vertical velocities (with the mean adjusted to 0 m s^{-1} and corrected for large-scale trends) during the cloud observation time of 16 minutes were found to be similar at the stratocumulus cloud base (observed with the Doppler lidar) and top (observed with ACTOS), with standard deviations of 0.23 m s^{-1} for ACTOS and 0.21 m s^{-1} for WiLi. This is an important fact for Doppler-lidar studies of stratocumulus clouds, because it implies that Doppler lidars are suitable to characterize the turbulence characteristics of entire stratocumulus cloud layers. From the vertical-velocity observations of WiLi and ACTOS also integral length scales were derived which were in the range from 38 m (ACTOS) to 45 m (WiLi). The observations will be further discussed in an upcoming publication (Seifert et al., 2017)

Furthermore, a combination of lidar and microwave radiometer data has been used to infer the height of the stable nocturnal boundary layer from aerosol-induced lidar backscatter variance and microwave radiometer derived potential temperature profiles (Saeed et al., 2016).

5 3.3 Thermodynamic properties of the atmosphere

Besides wind vectors, profiles of atmospheric temperature and humidity are the main drivers of numerical weather forecast-models and key for the verification of climate and Earth system models. An overview of their importance and the requirements set to observing systems is presented in Wulfmeyer et al. (2015). For models explicitly resolving turbulent processes (such as the HD(CP)² model), it is important to capture small-scale water vapour and thermodynamic stability fluctuations, which can trigger convection. Evaluation as well as data assimilation procedures for these models require advancements in measurement accuracy as well as in spatial and temporal resolution.

From the multi-sensor observations available for the HOPE-Jülich experiment, Steinke et al. (2015) investigated the comparability and range of applicability of various sensors for the determination of the integrated water vapour (IWV). As can be seen in Figure 8, in general a good agreement was found between the IWV observations from Global Positioning System (GPS) stations (Gendt et al., 2001), microwave radiometer, Sun photometer, and radiosonde. The systematic difference and standard deviation were derived to be approximately 0.4 kg m⁻² and 1 kg m⁻², respectively, but the performance and availability of each technique varies by means of meteorological conditions and time of the day. Spaceborne observations of the IWV from MODIS generally showed a bias toward lower values, which most probably results from difficulties in the discrimination of clear and cloudy scenes from the satellite data. IWV observations are compared to ICON simulations with 156-m horizontal resolution. A case study reveals that the diurnal cycle of IWV variability of the model matches well with the high-temporal-resolution microwave radiometer measurements, given a slight bias toward lower values in the model simulations, and that the spatial covariances for distances on the kilometer scale are comparable in observations and model.

A technique that is considered to provide accurate, continuous, height-resolved observations of the water vapour mixing ratio is the Raman lidar. Nevertheless, the stability of the system calibration is still subject of research and may depend on the design of specific systems. Based on observations with the Raman polarization lidar Polly^{XT} at supersite KRA and of BASIL at supersite JUE, Foth et al. (2015) presented a calibration technique that uses the integrated water vapour of a co-located microwave radiometer to provide calibration data for the lidar observations. The result is an automatically generated time-height cross section of the water vapour mixing ratio, as it is shown in Figure 9 for KRA for the April 2013 during HOPE-Jülich. As can be seen, lidar observations are only available at nighttime and only from the ground to the base of optically thick clouds. In a sophisticated approach, these data gaps will in future be filled with values obtained from an optimal-estimation scheme that considers the spatio-temporal evolution of both the integrated water vapour from the microwave radiometer and the vertical profiles of water vapour mixing ratio from the lidar (Foth et al., 2016). A similar methodology was also applied to the JUE BASIL and microwave radiometer data by Barrera-Verdejo et al. (2016) who could show the benefits

of sensor synergy in terms of an increase in information content in the regions where lidar data is not available. Barrera-Verdejo et al. (2016) similarly showed the positive impact of combining Rotational Raman Lidar measurements of BASIL with microwave radiometer observations for improving the temperature profile above the boundary layer.

Based on scanning measurements with the water-vapour DIAL of IPM made during HOPE-Jülich, Späth et al. (2016) (see Sect. 2.1.1) presented a detailed study of the 3-dimensional structure of the water vapour field between the supersites HAM, KRA, and JUE with a range resolution of 30-300 m and a temporal resolution in the range of 10 s for each profile. Full conical scans (360° in azimuth) around the site to characterize the water vapour field at a defined elevation angle took 15 min. Such observations provide valuable information for improving our understanding of land-atmosphere exchange processes as different types of land cover results in different evapo-transpiration and thus moisture in the CBL.

10

3.4 Microphysical properties of aerosols and clouds

The retrieval and evaluation of microphysical properties of aerosols, clouds, and precipitation from ground-based remote sensing observations is a crucial task. In-situ observations do provide much higher accuracy but for the long-term evaluation of the performance of operational weather forecast models and the microphysical parameterizations therein continuous datasets are required. In particular the HOPE-Melpitz campaign provided the opportunity to relate in-situ observations of warm-cloud microphysical properties and of aerosol properties from ACTOS to the respective parameters observed with ground-based observations of the LACROS facility. Case studies are presented in the following that document the simultaneous ground-based remote-sensing and in-situ observations of a stratocumulus layer and of the aerosol properties in the lower troposphere, respectively.

20 Aerosol particles act as nuclei for cloud droplets and ice crystals and are thus a prerequisite for the formation of clouds. Lidar is a promising tool to provide estimates of the concentration of cloud droplet condensation nuclei (CCN) and ice nucleating particles (INP) (Mamouri and Ansmann, 2016). During HOPE-Jülich and HOPE-Melpitz the Raman polarization lidar Polly^{XT} was continuously operated to provide information on the vertical aerosol structure in the planetary boundary layer and the troposphere. HOPE-Jülich was the first time a Raman polarization lidar provided a continuous data set of the calibrated attenuated backscatter coefficient at three wavelengths. Amongst other parameters, the dominating type of aerosol particles present in each observed volume was derived by a newly developed target classification, as is explained by Baars et al. (2017). Figure 10 shows an example of the aerosol target classification for three consecutive days from 24 to 26 April 2013 (IOPs 6-8) during HOPE-Jülich. Frequently large, non-spherical particles, probably dust or pollen particles that were emitted in the vicinity of the site have been monitored. The occurrence of these aerosol types is correlated with the development of the planetary boundary layer and they first appear close to the ground and are slowly dispersed into the boundary layer in the course of the day, as can be seen for 24 and 25 April in Figure 10. Baars et al. (2017) in addition present a case study that shows visual evidence of the dispersion of dust from the near-by open pit coal mine of Inden, west of the KRA site. With increasing distance from ground, the particles frequently grow by hygroscopic growth, leading to the presence of large,

30

spherical particles, as it was the case on 25 and 26 April. The mask also helps to identify whether a cloud layer was within or detached from the planetary boundary layer aerosol. Overall, the classification of cloud particles solely on the lidar observations is difficult. This will be overcome in a future step, by merging the multi-wavelength aerosol classification with the Cloudnet target classification presented in Illingworth et al. (2007).

5 Retrievals of microphysical aerosol properties, such as CCN concentration, from lidar observations, as well as retrievals of the ambient scattering properties of an aerosol population measured in-situ are still subject to large uncertainties. In-situ observations of aerosol properties are usually performed under dry conditions and inlets are limited by a maximum cut-off size of an aerosol distribution. During HOPE-Melpitz, both in-situ aerosol observations as well as lidar observations of Polly^{XT} were available. Figure 11 presents the relationship of the backscatter coefficient observed with Polly^{XT} and the respective extinction coefficient obtained from the in-situ aerosol observations of ACTOS as derived by Düsing et al. (2017). Based on the low-humidity (dry-state) in-situ aerosol measurements of ACTOS, the ambient extinction coefficient was obtained at wavelengths of 355, 532, and 1064 nm using a Mie model and a hygroscopic-growth correction. 13 data points derived for different altitudes and conditions on 14 and 17 Sept. 2013 (IOPs 20 and 21; see Table 4) are included in Figure 11. Each in-situ data point is based on all (and at least one) 120-s aerosol particle number size distributions recorded during a period of flight at a constant height. Averaging times for the lidar observations varied between 30 and 60 minutes. A linear relationship with significant R^2 values was derived between the modelled in-situ and remote-sensing extinction coefficients. For 355 nm 54% of all cases agree within the uncertainties and for 532 nm 55% of the cases. On average, the model underestimates the measured extinction coefficients for 355 nm by 3.5% and overestimates the measurements by 7.9% at a wavelength of 532 nm. Correlation coefficients are 0.944 and 0.947, respectively. This shows that the ambient aerosol extinction coefficient can well be derived from in-situ measurements given the extensive instrumentation for microphysical and chemical aerosol characterization that is available at the Melpitz field site.

During HOPE-Jülich the availability of CCN was investigated using an aerosol model. The approach presented by Hande et al. (2016) used the COSMO-MUSCAT model to simulate the generation and transportation of aerosols over Germany during the campaign. From the simulation results, a parameterisation of the CCN concentration was derived which can be applied also to other climatological regions and different aerosol regimes. Even though the simulated aerosol properties were evaluated against in-situ observations of aerosol particle size distributions at Melpitz, no evaluation of the CCN parameterisation against measurements was performed. This emphasizes the need to improve remote-sensing techniques for the retrieval of CCN profiles as the one of Mamouri and Ansmann (2016).

At the beginning of the first Phase of HD(CP)² no operational microphysical retrieval of the effective radius of cloud droplets from ground-based remote sensing observations was available within the project. As a first step towards an evaluation dataset for numerical weather forecasts, it was decided to apply the retrieval technique of Frisch et al. (2002) to the LACROS observations by implementing it into the processing framework of Cloudnet. The technique is based on vertically-pointing measurements from a millimetre-wavelength cloud radar and a microwave radiometer and produces height-resolved estimates of cloud particle effective radius and liquid water content. In addition, liquid water content profiles are produced operationally

within Cloudnet (Illingworth et al., 2007), assuming either adiabatic profiles of liquid water content (LWC) between the lidar-derived cloud base and the radar-derived cloud top or scaled-adiabatic profiles for which the adiabatic liquid water content is scaled to fit the liquid water path observed with the microwave radiometer (Merk et al., 2016).

The implemented Frisch-2002 retrieval of cloud droplet effective radius and the Cloudnet retrieval of the adiabatically scaled LWC were evaluated against in-situ observations of ACTOS for a stratocumulus deck observed simultaneously by ACTOS and LACROS during the HOPE-Melpitz campaign on 22 September 2013 (IOP 22) from 09:59-10:16 UTC, as is shown in Figure 12. During the time period, ACTOS constantly flew horizontal legs of 2 km length in cross-wind direction in a distance of about 500-m upwind of the LACROS site. Time-height cross-sections from the continuous LACROS observations as shown in Figure 12 (a) and (b) will be available in the SAMD database (Sect. 2.2.3) for entire HOPE-Jülich and HOPE-Melpitz. The comparisons of the average vertical profiles of LWC and cloud droplet effective radius observed with ACTOS and retrieved with LACROS are shown in Figure 12. It can be seen that ACTOS probed mainly the mid-upper part of the cloud layer. Both, the observations of the LWC of the cloud droplet effective radius of ACTOS and LACROS (Figure 12a) are within the range of one standard deviation, as is shown by the horizontal error bars. Beside the found absolute differences, the profiles of LWC and effective radius retrieved from the LACROS observations deviate more strongly from those of ACTOS toward cloud top. A possible explanation for the observed discrepancies is the temporal variability of the LWC and effective radius in the cloud-top region as is shown in Figure 12 (a) and (b). Also, ACTOS was not flying directly above the LACROS site. Considering the applied retrieval of Eq. 5 in Frisch et al. (2002), also the assumption of a certain shape of the size distribution and of a cloud droplet number concentration can introduce biases. The application of the co-located observations of ACTOS and LACROS for the evaluation of ground-based retrievals will be discussed in an upcoming publication (Seifert et al., 2017).

The accurate representation of the ice phase in numerical models is a crucial task since cold rain is the main driver of precipitation formation at midlatitudes (Mülmenstädt et al., 2015). The continuous observations of the LACROS supersite during HOPE-Jülich enabled to obtain statistical information about the primary ice production in stratiform midlevel mixed-phase cloud layers. Figure 13 shows an overview about the ice water content and ice-to-total mass ratio of all mixed-phase cloud layers that were identified from the HOPE-Jülich observations. In these plots the method for measurement of ice formation efficiency of Bühl et al. (2016) is used, which selects supercooled thin stratiform cloud layers with a turbulent mixed-phase (liquid-dominated) cloud top of a vertical extent of less than 380 m. In this way, non-linear ice formation effects like ice multiplication or splintering are avoided and, thus, do not affect the statistics. IWC is measured 60 m below the base of the mixed-phase layer, where an observation of the falling ice particles is possible without influence of water droplets or turbulent motions. LWC are mean values of the scaled-adiabatic approach (Merk et al., 2016) averaged over the complete height of the shallow mixed-phase top layer of the cloud where liquid water is present. As shown in Figure 13, the ice water content of clouds with top temperatures above $-10\text{ }^{\circ}\text{C}$ was in general lower than 10^{-4} g m^{-3} . At temperatures below $-15\text{ }^{\circ}\text{C}$, values of the ice water content vary around 10^{-3} g m^{-3} . The ice-to-liquid mass ratio decreases from 10^{-2} to 10^{-5} for temperatures increasing from -40 to $0\text{ }^{\circ}\text{C}$. The plots thus quantify how ice formation becomes more efficient with decreasing temperature. The colour-coded data points in Figure 13 provide in addition the radar-observed linear depolarization ratio of the observed

ice particles, which is a proxy for the particle shape. Values of around -20 dBZ ($-10\text{ °C} < T < -5\text{ °C}$), -30 dBZ ($-20\text{ °C} < T < -10\text{ °C}$), and -25 dBZ ($T < -20\text{ °C}$) indicate needle-like, dendritic, and bullet-rosette-like shapes, respectively (Bühl et al., 2016; Myagkov et al., 2016). Knowing about the relationship between ice water content, liquid water content, temperature, and shape of freshly formed ice crystals is an important step towards new approaches for the evaluation of ice formation schemes in numerical weather forecast models. This will also be a task of the second phase of HD(CP)².

3.5 Macrophysical cloud & precipitation properties

The combination of scanning polarimetric X-band Doppler rain radars, vertically pointing micro rain radars (MRR) and a ground-based network of disdrometers and rain gauges provided an excellent opportunity to validate the Doppler rain radar ability to infer the spatial variability of quantitative precipitation properties from polarimetric radar reflectivities. Xie et al. (2016) performed a detailed analysis of all precipitation observations under different synoptic conditions. As an example, Figure 14 shows a time series of the surface precipitation rates estimated from measurements of three Doppler rain radar compared to the in-situ observations from seven disdrometers (partly from TR32 and TERENO projects), averaged over the disdrometer locations. The authors note that rainfall accumulations at the daily and even hourly scale were surprisingly consistent between the different observations of rain gauges, disdrometers and X-band radar, at least for the low-intensity rainfall events (of $0.5 - 20\text{ mm day}^{-1}$) prevalent during HOPE-Jülich. The correlation was found to be better than 0.93. The two near-by radars (KiXPol and JuXPol) showed slightly better agreement than the 50 km remote radar BoXPol, which is explained by its correspondingly larger field of view and associated beam-filling errors. Xie et al. (2016) also managed to associate distinct microphysical processes for rain formation like coalescence, size-sorting and riming/aggregation with the measured polarimetric properties of the hydrometeors. These polarimetric fingerprints serve as very useful information for process understanding of rain formation and model validation (Trömel and Simmer, 2012)

Ground-based cloud photography provides the most detailed qualitative information on cloud patterns at high spatial and temporal resolution. Consequently, up to six sky imagers were operated in the SKY network during HOPE-Jülich. The combination of several imagers allows also for a quantitative retrieval of the spatial cloud structure. Beekmans et al. (2016) presented an approach for a spatial cloud reconstruction by using two hemispheric sky imagers in a stereoscopic setup. They combined a dense stereo correspondence technique and a large-scale stereo setup to derive 3D cloud geometries. Obviously, such a stereoscopic cloud reconstruction is best suited for convective clouds that exhibit strong 3D spatial features. Important aspects of such a technique include an accurate camera calibration (internal projection and camera orientation in space), precise synchronization, similar radiometric properties, and successful stereo matching on the rather fuzzy (diffuse) cloud images. As an example, Figure 15 shows the determination of a cross section (panel d) from a reconstruction from a cumulus cloud (panel a). It was found that the near-zenith cloud base height is very well reproduced in comparison to lidar observations, yielding errors between five to ten percent for low to mid-altitude cumuliform clouds. In general, Beekmans et al. (2016) provided a

complete approach including geometric and radiometric corrections to obtain the spatial cloud envelope geometry for the cloud sides facing the sky imagers. Together with 3D cloud information from scanning active systems such data will be very valuable for cloud reconstruction and radiation closure studies.

5 4 Application of HOPE observations in modelling activities

In the previous section, results of the HOPE observations were presented by means of a summary of the different studies covering a large range of meteorological processes from land-surface-atmospheric boundary layer exchange, cloud and precipitation processes to the sub-grid variability and microphysical properties of clouds and precipitation. Within this section the application of these results for the evaluation of the newly developed ICON model in LES mode but also to other LES and small-scale GCMs will be summarized. A detailed overview about the setup of the different models can be found in Heinze et al. (2017). In general, ICON was run in LES mode on a daily basis. Thus, usually the model was initialized at 00 UTC and calculations were performed for a period of 24 hours. The lateral boundaries for the ICON runs were provided by the COSMO-DE model (Baldauf et al., 2011), which is one of the operational models of the German Meteorological Service (DWD). Within the boundaries of COSMO-DE, covering full Germany and the Netherlands as well as parts of the other neighbouring countries, three ICON domains, only slightly smaller than the COSMO-DE domain (47.6° N -54.6° N, 4.5° E -14.5° E), are nested, having horizontal resolutions of 625 m, 312 m, and 156 m, respectively, and a vertical resolution of 150 layers within 21 km of height above ground. The simulation of 1 day takes approximately 12 days when run on 7200 computing cores and creates 50 TB of output data. LES runs of other models at spatial resolutions in the range of 50 m were reduced to smaller areas around the HOPE-Jülich region and periodic boundary conditions were applied to these models. Those were the models ICON-SI (ICON semi idealized), PALM (PARallelized Large-eddy simulation Model 4.0; Maronga et al. (2015)) and DALES (Dutch Atmospheric LES; (Heus et al., 2010)).

Given the requirements on computational time and storage space the simulation days were chosen according to the appropriateness of the present weather conditions for the evaluation goals. A list of the HOPE days for which ICON runs are already available is provided in Table 5. It should be noted that the number of modelled HOPE days is subject to change in the future and that ICON runs for dates not covered by HOPE were also already performed but are not shown in here. The HOPE days selected for ICON runs cover a wide range of meteorological conditions, from clear-sky days for the evaluation of convective processes in the planetary boundary-layer to days on which frontal passages accompanied by large-scale precipitation occurred. Most evaluation efforts were so far performed in a study of Heinze et al. (2017), but also others already made use of the extensive observational dataset. The studies available so far are discussed below.

30

4.1 Examples of model-observation inter-comparisons

The observational studies presented in Section 3 demonstrate well that large efforts are being taken to make observations suitable for the initialization and the evaluation of numerical weather prediction (NWP) models and to provide process studies that are essential for their improvement. The high temporal resolution of the HOPE dataset allows an analysis beyond the mean, which offers new opportunities to improve the simulation of boundary layer dynamics. Vertical profiles of higher-order moments (variances and turbulent fluxes) can be derived (Behrendt et al., 2015; Van Weverberg et al., 2016) which are essential to advance higher-order closure parameterizations of turbulent transport schemes in numerical models. Recent large-eddy simulation studies analysed the underlying sources and sinks of such prognostic higher-order moment equations for the cloud topped boundary layer (Heinze et al., 2015) and precipitating shallow cumulus regime (Schemann and Seifert, 2017). While these studies underline the importance, more robust conclusions are achieved by combining synoptically realistic model simulations with accompanying observational studies.

Nevertheless, operating a forecast model at scales that are small enough to resolve the different supersites of the HOPE-Jülich campaign puts certain requirements on the capabilities of the model. When the model resolution is between large-eddy simulations (with resolved energy-containing turbulence) and mesoscale simulations (no turbulence resolved), the model is operating in the so-called “grey zone” where more-sophisticated physical parameterizations (e.g. for boundary-layer turbulence or cloud microphysics) might be needed. To what extent the parameterization of turbulence and shallow convection is still necessary has been one of the key subjects of HD(CP)². Based on HOPE-Jülich observations, the grey zone was investigated in a study of Barthlott and Hoose (2015) who performed simulations with the COSMO model at horizontal resolutions ranging between 250 m and 2.8 km for six HOPE IOPs and one additional summertime case of the same year of 2013. From the kinetic energy spectra derived from the model output, it was found that the effective resolution (the minimum size of resolvable eddies) lies between 6 and 7 times the nominal resolution. Finer resolutions improved the representation of boundary-layer thermals, low-level convergence zones and gravity waves, but the effect on the temporal evolution of mean precipitation was rather weak. However, due to sensitivities of the rain intensities to model resolution, differences in the total rain amount of up to +48% occurred. Whereas the location of rain was rather similar at all model resolutions for the springtime cases of HOPE with moderate to strong synoptic forcing, the summertime case with airmass convection showed strong differences between the different resolutions with better agreement to the observed precipitation amount at the highest resolution of 250 m.

A major goal of HD(CP)² has been to use high-resolution modelling to derive parametrizations for climate models and general circulation models. In this respect the vertical cloud overlap parametrization is of high interest as it strongly influences the distribution of energy. In the past, such parametrizations have only been tested against observations on a global scale or for deep convective clouds. For the first time, Corbetta et al. (2015) investigated cumuliform cloud overlap for several boundary layer cloud cases including HOPE and compared it with the results from LES runs of the DALES model. Gridded time-height data from Cloudnet were used to derive cloud fraction masks at various temporal and vertical resolutions. The authors investigated the overlap ratio, i.e., the ratio of the cloud fraction by volume to the vertically averaged cloud fraction by area of

a grid box, as a function of the vertical resolution of the grid box. Cumuliform-cloud overlap ratios were found considerably underestimated by the LES model. For model-layer depths of less than 100 m, the modelled cloud overlap deviated by less than 7% from the observed one. The difference gradually increases to 15% for layer depths of 500 m and approached 20% for larger layer depths. Stratiform clouds were found to be better reproduced by the model, compared to cumuliform clouds. Interestingly, the simulated and observed decorrelation lengths found for this type of clouds are smaller (~300 m) than previously reported (>1 km). The authors conclude that the inefficient overlap found at large vertical scales has the potential of significantly affecting the vertical transfer of radiation in large-scale GCM, because usually volume and area cloud fractions are assumed to be identical. The study can thus help to improve corresponding sub-grid parametrizations.

The evaluation of actual LES simulations of the HOPE-Jülich area was done by Heinze et al. (2016) who performed simulations with PALM and UCLA-LES (University of California, Los Angeles Large-Eddy Simulation model, Stevens et al. (2005)) at up to 50 m horizontal resolution over the HOPE domain for a 19-day time period in order to capture a variety of different atmospheric and especially boundary layer conditions. The general weather pattern was reproduced in 80% of the cases. Also cloud types usually agree well with observations. Resulting turbulence characteristics and boundary layer heights have been compared to observations from active remote sensing (Doppler lidar and aerosol lidar) and from in-situ radiosonde observations as proposed by Schween et al. (2014). Figure 16 exemplarily shows the temporal evolution of the boundary layer height as derived from different model runs and from observations. The 2-hour (12-14 UTC) mean boundary layer depth derived with the PALM model agreed within 400 m to the different observation methods and to the COSMO-DE run at 2.8-km resolution. The found differences are pointing to problems in the representation of ABL features in the LES, and should be subject of further investigations. Please note that the criterion of model-based ABL depth is also subject to uncertainties which is explained further by Milovac et al. (2016) who found similar deviations between measurements and observations as found by Heinze et al. (2016). Heinze et al. (2016) further compared the observed turbulence characteristics of the ABL with the LES model. Observed and modelled profiles of the vertical-velocity variance agreed in their shape with the modelled values being in the range of uncertainty of the observations and showing slightly higher values throughout the boundary layer. Modelled profiles of potential temperature variances were found to be lower than the TRRL observations. For humidity variance, agreement within the uncertainty range was found in the lower and mid-CBL between measurements and LES models. But the modelled variance peaks at the CBL top showed an under-estimation when compared with observations. Significant differences with respect to results from coarser resolved COSMO simulations were not reported. This might in part be due to the so-called semi-idealized set up with periodic boundary conditions and a homogeneous surface forcing. The authors also conclude that the simulated longwave and shortwave surface fluxes simulated with the LES model can be seen as representative in comparison to respective observations at 5 different sites in the HOPE area. The peak shortwave heat flux in the LES and COSMO-DE tends to be overestimated compared to the weighted average, whereas the longwave heat flux tends to be underestimated.

Furthermore, within the Synthesis Module of HD(CP)², high-resolution ICON runs with 625-m, 312-m, and 156-m resolution were extensively evaluated against datasets collected during HOPE-Jülich and from other sources (Heinze et al., 2017). It was

found that the highest-resolved ICON-LES model matches much better the observed variability at small- to meso-scales than the coarser-resolved model runs or the reference model COSMO-DE with its 2.8-km horizontal resolution. It was demonstrated that the simulated turbulence profiles of the vertical velocity approach the observed ones for an increase in the ICON horizontal resolution from 625 m to 156 m. Differences between observed and modelled variance profiles of potential temperature and specific humidity were much larger, which was explained by the absence of surface and soil moisture inhomogeneity in the model setup. The integrated water vapour of all models matched the range of values from the observations, but the temporal variability at short timescales as it was observed with microwave radiometer on a 1-s basis was only reproduced by the 156-m resolution run of ICON. From direct comparisons between modelled and continuous ground-based observations of the cloud field during HOPE-Jülich it was however found that convective boundary layer clouds are under-represented in the model, even though the evaluation of the cloud fields on a larger scale, i.e. in comparison to satellite observations, showed that clouds are well represented in the model. Heinze et al. (2017) concluded that, despite the given potential for further improvement of the ICON-LES model, it already fits well to the purpose of using its output for parameterisation development.

Regarding the application of HOPE observations for the initialization of NWP models, a first attempt was recently reported by Adam et al. (2016) who concentrated on the 24 April 2013 (IOP 6). In their study the authors assimilated lower-tropospheric temperature profiles from the TRRL, reaching from about 500 to 3000 m above ground, into the Weather Research and Forecasting (WRF; Skamarock et al. (2008)) model using a 3D-variational method (Barker et al., 2004). The WRF model was covering Central Europe with 57 vertical levels and 3-km horizontal resolution. The assimilation of the temperature profiles from the TRRL in addition to the assimilation of conventional data including zenith total delay integrated water vapour field from the Global Navigation Satellite System and operational radiosonde data were found to improve the agreement of measured boundary layer height and temperature gradient to the modelled values. Nine hours after the assimilation of TRRL data was initialized, already an area of 100 km in radius around the HOPE-Jülich area was affected, showing a temperature deviation from the conventional run of up to 2.5 K at 2.5 km height above sea level. Similar impacts can also be expected for the assimilation of profiles of water vapour mixing ratio from continuous lidar observations, as was found in an earlier study of Grzeschik et al. (2008).

25 **5 Summary & conclusions**

The HD(CP)² Observational Prototype Experiment HOPE provided an unprecedented data set on the spatiotemporal structure of surface and boundary layer energy fluxes, temperature, humidity, aerosols, clouds and precipitation fields along a variety of weather situations. All data that have been measured by the official HD(CP)² partner institutes are stored in the HD(CP)² Data Archive Centre SAMD, and are publicly available. Currently, evaluation of the ICON model is performed both on small spatiotemporal scales based on the HOPE data and over the entire domain of Germany exploiting supersite, satellite, and radar data. The extensive data base enable studies beyond pure model evaluation with a large potential for process studies on boundary layer fluxes, the formation of clouds and precipitation, cloud-aerosol interaction and on many more aspects.

With the large number of in-situ and Doppler wind lidar instruments coherent structures in the surface-near boundary layer wind fields and characteristic integral scales have been identified, and have been related to the type of external forcing. For the first time to our knowledge, TRRL demonstrated its capability to resolve the temperature inversion layer at the top of the ABL during daytime, which is key information for future process studies. Similarly, vertical temperature fluctuations have been observed for the first time by means of rotational Raman lidar measurements. It turned out that a temporal resolution of 10 s was sufficient to resolve turbulence structures down to the inertial sub-range from the mixed layer to the entrainment zone. Observed statistics of vertically resolved temperature fluctuations up to the forth-order moment provide important information on boundary layer dynamics and thermodynamics. The combination of daytime temperature and humidity profiles from Raman lidar and water vapour DIAL measurements with Doppler lidar measurements was used to obtain turbulent flux profiles in the convective boundary layer. In general, the combination of vertically resolved (lidar) and vertically integrated (microwave radiometer) and in-situ (radiosondes) measurements of the atmospheric humidity has produced a unique 3D field that together with wind and temperature measurements will serve as a solid constraint for the evaluation of high-resolution models. These results confirm the importance of high-resolution thermodynamic profiles for weather and climate research as demonstrated in Wulfmeyer et al. (2015). Surface solar and thermal radiation budget measurements complement the energy budget observations. A high-resolution pyranometer network produced statistics on spatiotemporal solar irradiance correlations for different sky conditions.

A comparison of turbulence measurements near cloud top from aircraft in situ measurements and from cloud base by lidar measurements revealed similar statistical properties, which points to a vertically homogeneous turbulence structure inside stratocumulus clouds.

Continuous operations of most of the instruments for two months made it possible to identify atmospheric variability from the micro- to the mesoscale. A long-term comparison of integrated water vapour from radiosondes and from ground-based and satellite remote sensing shows a generally good agreement but also revealed a bias of the spaceborne measurements towards lower values. Lidar observations of the aerosol profiles have been translated into the dominant aerosol type within each measurement volume. Such aerosol target classifications showed the hygroscopic growth of spherical aerosol particles under humid conditions as well as the presence of large non-spherical dust particles that were emitted from near-by sources. It turned out that the closure of in-situ observations and remote sensing of aerosol microphysical properties is feasible when an extensive aerosol in-situ characterisation is available. A respective closure of cloud microphysical properties remains challenging due to uncertainties stemming from required assumptions on the particle size distribution and from spatiotemporal averaging. Cloud liquid water content profiles derived in-situ and with remote sensing, however, were found to agree well. Continuous observations of mixed phase clouds from a combination of active and passive remote sensing shows that the ratio of ice to liquid water increases with decreasing cloud top temperature, which serves as an important information for the evaluation of ice formation parameterizations in cloud modelling.

Macrophysical cloud structures like cloud vertical dimension, cloud cover, cloud type, precipitation fields have been continuously observed with lidar, radar and sky imager. Large-scale precipitation patterns together with the dominant process

type for precipitation formation were observed with polarimetric Doppler precipitation radars. Three-dimensional cloud morphology has been retrieved from sky imagers in a stereoscopic setup. Thus, a uniquely high resolved data set on cloud structural properties has been achieved during HOPE.

With the completion of the high-resolution ICON LES model a vast number of model evaluation work is currently in progress.

5 First evaluation studies based on HOPE data have shown general agreement between observed and modelled boundary layer height, turbulence characteristics, and cloud coverage, but also point to significant differences that deserve further investigations, both from the observational and from the modelling perspective. Although the meteorological conditions which were prevalent during HOPE-Jülich and HOPE-Melpitz enabled the collection of a broad set of observations, it is obvious that the experimental coverage of the atmospheric boundary layer requires ongoing measurement efforts. In particular the
10 continuous observations from the German supersites will contribute to these efforts. The supersites JOYCE, KIT, and LACROS that have been deployed during HOPE-Jülich continue their long-term measurements at their base institutes and will contribute to further process and model evaluation studies in conjunction with further national and international supersites like Barbados (13.2° N, 59.4° W), Cabauw, the Netherlands, (51.9° N, 4.9° E), Lindenberg, Germany, (52.2° N, 14.1° E), Zugspitze mountain, Germany, (47.4° N, 11° E) as well as mobile facilities from the US (ARM) and Germany (mobile deployments of
15 the KIT cube, LACROS) under specific climatological and meteorological conditions.

Future work will take advantage of the synergy of the different active and passive remote sensing measurements. For instance, Doppler lidar and polarimetric radar measurements may link dynamical forcing (up and downdrafts) with microphysical processes (riming, coagulation, ice formation). The cloud radars of JOYCE, KITcube and LACROS were occasionally operating in a synchronized scan mode. Together with vertically pointing and scanning microwave radiometer data, three-
20 dimensional distributions of cloud liquid water may be constructed, and may get even further refined from cloud structure stereoscopy from synchronized sky imager data. Radiation closure studies will be performed based on observed and modelled spatial cloud structures and observed surface radiation budget measurements. High-resolution irradiance data can be used to build stochastic irradiance simulators for specific cloudy sky conditions, which in turn can be used to construct realistic cloud induced solar radiation variability. Combined measurements of temperature, humidity, and vertical wind fluctuations in the
25 PBL under different meteorological conditions will provide important statistical information for improved turbulence parameterizations. HOPE also demonstrated the future potential of the synergy of scanning wind, temperature, and water-vapour lidar systems for 3D studies of land-atmosphere exchange and ABL entrainment in heterogeneous terrain. HOPE data may also reveal to what extent variations in aerosol concentrations and thus in CCN and IN concentrations have an effect on cloud and ice formation compared to dynamical forcing.

30 In future, HOPE data will continue to contribute to the development, evaluation and improvement of high-resolution NWP and LES models because the data will be available via the Standardized Atmospheric Measurement Data (SAMD) data base which fulfils the needs of in particular model experts. Focused on the ICON development and on the collection of observational data for model evaluation, Phase 1 of HD(CP)² set the starting point for an ongoing, synergistic use of HOPE and other observational data by the modelling community. In Phase 2 of HD(CP)², which started in 2016, HD(CP)² participants are

already making use of these observations. For instance, a project on boundary layer clouds will confront ICON with HOPE data for different cloud regimes at different spatiotemporal scales. A project addressing fast cloud adjustment to aerosols will exploit remote-sensing and in-situ observations of aerosol and cloud properties to evaluate the susceptibility of the model performance to different representations of aerosol in the model, e.g., to variations in the concentration of nuclei for cloud droplets or ice crystals. A project on the effects of surface heterogeneity e.g. uses the HOPE observations to challenge the applicability of the Monin-Obukhov Similarity Theory (MOST) and the reproduction of the vertical boundary layer structure and turbulence on small scales. Other projects apply the observations of the 3D water vapour fields and the cloud microphysical properties derived with Cloudnet for the development of convection parameterizations, just to mention a few.

Thanks to the valuable efforts of the community of observers during the HOPE campaigns and given its open-access availability in the SAMD database (See Sect. 2.2.3) the HOPE dataset can serve as excellent tool for the model evaluation and initialization community.

Acknowledgements

The work summarized in this review was mainly carried out in the project HD(CP)² funded by the German Ministry for Education and Research. We specifically acknowledge the HD(CP)² projects 01LK1212A (University of Hohenheim), 01LK1209D (University of Leipzig), 01LK1209B (FZJ), 01LK1209C and 01LK1212C (TROPOS), 01LK1212F and 01LK1204B (KIT), 01LK1219A and 01LK1210A (University of Bonn), 01LK1203B (University of Hannover), 01LK1203A (MPI Hamburg). We also refer to all acknowledgements in the publications cited in section 3.

HOPE is particularly grateful to the Research Center Jülich and RWE Power AG (Hambach) that provided generous logistic support during the Jülich campaign. We thank the Transregional Collaborative Research Centre 32 "Patterns in Soil-Vegetation-Atmosphere Systems - Monitoring, Modelling and Data Assimilation" for contributing their valuable rain observation research infrastructures to the Jülich campaign.

The universities of Cologne and Bonn as well as TROPOS secured intense radiosonde observations from internal budgets. Raman lidar system BASIL were funded on the basis of a specific cooperation agreement between Scuola di Ingegneria - Università degli Studi della Basilicata, TROPOS and MPI Hamburg.

We appreciated the provision of four Sun photometers for HOPE-Jülich and one device for HOPE-Melpitz by Goddard Space Flight Center, Greenbelt, MD, USA.

References

- Adam, S., Behrendt, A., Schwitalla, T., Hammann, E., and Wulfmeyer, V.: First assimilation of temperature lidar data into an NWP model: impact on the simulation of the temperature field, inversion strength and PBL depth, *Quarterly Journal of the Royal Meteorological Society*, 142, 2882-2896, 10.1002/qj.2875, 2016.
- 5 Baars, H., Kanitz, T., Engelmann, R., Althausen, D., Heese, B., Komppula, M., Preißler, J., Tesche, M., Ansmann, A., Wandinger, U., Lim, J. H., Ahn, J. Y., Stachlewska, I. S., Amiridis, V., Marinou, E., Seifert, P., Hofer, J., Skupin, A., Schneider, F., Bohlmann, S., Foth, A., Bley, S., Pfüller, A., Giannakaki, E., Lihavainen, H., Viisanen, Y., Hooda, R. K., Pereira, S. N., Bortoli, D., Wagner, F., Mattis, I., Janicka, L., Markowicz, K. M., Achtert, P., Artaxo, P., Pauliquevis, T., Souza, R. A. F., Sharma, V. P., van Zyl, P. G., Beukes, J. P., Sun, J., Rohwer, E.
- 10 G., Deng, R., Mamouri, R. E., and Zamorano, F.: An overview of the first decade of PollyNET: an emerging network of automated Raman-polarization lidars for continuous aerosol profiling, *Atmos. Chem. Phys.*, 16, 5111-5137, 10.5194/acp-16-5111-2016, 2016.
- Baars, H., Seifert, P., Engelmann, R., and Wandinger, U.: Target categorization of aerosol and clouds by continuous multiwavelength-polarization lidar measurements, *Atmos. Chem. Phys. Discuss.*, Accepted for publication in the discussions, 2017.
- 15 Baldauf, M., Seifert, A., Förstner, J., Majewski, D., Raschendorfer, M., and Reinhardt, T.: Operational Convective-Scale Numerical Weather Prediction with the COSMO Model: Description and Sensitivities, *Monthly Weather Review*, 139, 3887-3905, 10.1175/mwr-d-10-05013.1, 2011.
- 20 Barker, D. M., Huang, W., Guo, Y.-R., Bourgeois, A. J., and Xiao, Q. N.: A Three-Dimensional Variational Data Assimilation System for MM5: Implementation and Initial Results, *Monthly Weather Review*, 132, 897-914, 10.1175/1520-0493(2004)132<0897:atvdas>2.0.co;2, 2004.
- Barrera-Verdejo, M., Crewell, S., Löhnert, U., Orlandi, E., and Di Girolamo, P.: Ground-based lidar and microwave radiometry synergy for high vertical resolution absolute humidity profiling, *Atmos. Meas. Tech.*, 9, 4013-4028, 10.5194/amt-9-4013-2016, 2016.
- 25 Barthlott, C., and Hoose, C.: Spatial and temporal variability of clouds and precipitation over Germany: multiscale simulations across the "gray zone", *Atmos. Chem. Phys.*, 15, 12361-12384, 10.5194/acp-15-12361-2015, 2015.
- 30 Beekmans, C., Schneider, J., Läbe, T., Stachniss, C., and Simmer, C.: Cloud Photogrammetry with Dense Stereo for Fisheye Cameras, *Atmos. Chem. Phys. Discuss.*, 2016, 1-29, 10.5194/acp-2016-319, 2016.
- Behrendt, A., Wulfmeyer, V., Riede, A., Wagner, G., Pal, S., Bauer, H., Radlach, M., and Späth, F.: Three-dimensional observations of atmospheric humidity with a scanning differential absorption Lidar, in: *SPIE Conference Proceedings, Remote Sensing of Clouds and the Atmosphere XIV, Volume 7475*, 2009.
- 35 Behrendt, A., Pal, S., Aoshima, F., Bender, M., Blyth, A., Corsmeier, U., Cuesta, J., Dick, G., Dorninger, M., Flamant, C., Di Girolamo, P., Gorgas, T., Huang, Y., Kalthoff, N., Khodayar, S., Mannstein, H., Trümmer, K., Wieser, A., and Wulfmeyer, V.: Observation of convection initiation processes with a suite of state-of-the-art research instruments during COPS IOP 8b, *Quarterly Journal of the Royal Meteorological Society*, 137, 81-100, 10.1002/qj.758, 2011.
- 40 Behrendt, A., Wulfmeyer, V., Hammann, E., Muppa, S. K., and Pal, S.: Profiles of second- to fourth-order moments of turbulent temperature fluctuations in the convective boundary layer: first measurements with rotational Raman lidar, *Atmos. Chem. Phys.*, 15, 5485-5500, 10.5194/acp-15-5485-2015, 2015.
- 45 Bhawar, R., Di Girolamo, P., Summa, D., Flamant, C., Althausen, D., Behrendt, A., Kiemle, C., Bossler, P., Cacciani, M., Champollion, C., Di Iorio, T., Engelmann, R., Herold, C., Müller, D., Pal, S., Wirth, M., and Wulfmeyer, V.: The water vapour intercomparison effort in the framework of the Convective and Orographically-induced Precipitation Study: airborne-to-ground-based and airborne-to-airborne lidar systems, *Quarterly Journal of the Royal Meteorological Society*, 137, 325-348, 10.1002/qj.697, 2011.
- 50 Bock, O., Bossler, P., Pacione, R., Nuret, M., Fourrié, N., and Parracho, A.: A high-quality reprocessed ground-based GPS dataset for atmospheric process studies, radiosonde and model evaluation, and reanalysis of HyMeX Special Observing Period, *Quarterly Journal of the Royal Meteorological Society*, 142, 56-71, 10.1002/qj.2701, 2016.

- Borowska, L., Zrnić, D., Ryzhkov, A., Zhang, P., and Simmer, C.: Polarimetric Estimates of a 1-Month Accumulation of Light Rain with a 3-cm Wavelength Radar, *Journal of Hydrometeorology*, 12, 1024-1039, doi:10.1175/2011JHM1339.1, 2011.
- 5 Bryan, G. H., Wyngaard, J. C., and Fritsch, J. M.: Resolution Requirements for the Simulation of Deep Moist Convection, *Monthly Weather Review*, 131, 2394-2416, doi:10.1175/1520-0493(2003)131<2394:RRFTSO>2.0.CO;2, 2003.
- Bühl, J., Engelmann, R., and Ansmann, A.: Removing the Laser-Chirp Influence from Coherent Doppler Lidar Datasets by Two-Dimensional Deconvolution, *Journal of Atmospheric and Oceanic Technology*, 29, 1042-1051, doi:10.1175/JTECH-D-11-00144.1, 2012.
- 10 Bühl, J., Seifert, P., Wandinger, U., Baars, H., Kanitz, T., Schmidt, J., Myagkov, A., Engelmann, R., Skupin, A., Heese, B., Klepel, A., Althausen, D., and Ansmann, A.: LACROS: the Leipzig Aerosol and Cloud Remote Observations System, *Proceedings of the SPIE 8890 conference on Remote Sensing of Clouds and the Atmosphere XVIII and Optics in Atmospheric Propagation and Adaptive Systems XVI*, Dresden, Germany, 2013, 889002-889002-889006,
- 15 Bühl, J., Seifert, P., Myagkov, A., and Ansmann, A.: Relation between ice and liquid water mass in mixed-phase cloud layers measured with Cloudnet, *Atmos. Chem. Phys. Discuss.*, 2016, 1-19, 10.5194/acp-2016-25, 2016.
- Corbetta, G., Orlandi, E., Heus, T., Neggers, R., and Crewell, S.: Overlap statistics of shallow boundary layer clouds: Comparing ground-based observations with large-eddy simulations, *Geophysical Research Letters*, 42, 8185-8191, 10.1002/2015GL065140, 2015.
- 20 Couvreur, F., Guichard, F., Redelsperger, J. L., Kiemle, C., Masson, V., Lafore, J. P., and Flamant, C.: Water-vapour variability within a convective boundary-layer assessed by large-eddy simulations and IHOP_2002 observations, *Quarterly Journal of the Royal Meteorological Society*, 131, 2665-2693, 10.1256/qj.04.167, 2005.
- 25 Crewell, S., Mech, M., Reinhardt, T., Selbach, C., Betz, H.-D., Brocard, E., Dick, G., O'Connor, E., Fischer, J., Hanisch, T., Hauf, T., Hünerbein, A., Delobbe, L., Mathes, A., and Peters: The general observation period 2007 within the priority program on quantitative precipitation forecasting: Concept and first results, *Meteorologische Zeitschrift*, 17, 849-866, 2008.
- Deardorff, J. W.: A numerical study of three-dimensional turbulent channel flow at large Reynolds numbers, *Journal of Fluid Mechanics*, 30, 41, 453-480, doi:10.1017/S0022112070000691, 1970.
- Di Girolamo, P., Summa, D., Lin, R. F., Maestri, T., Rizzi, R., and Masiello, G.: UV Raman lidar measurements of relative humidity for the characterization of cirrus cloud microphysical properties, *Atmos. Chem. Phys.*, 9, 8799-8811, 10.5194/acp-9-8799-2009, 2009.
- 35 Di Girolamo, P., Cacciani, M., Summa, D., Scoccione, A., De Rosa, B., Behrendt, A., and Wulfmeyer, V.: Characterization of Boundary Layer Turbulent Processes by the Raman Lidar BASIL in the frame of HD(CP)2) Observational Prototype Experiment, *Atmos. Chem. Phys. Discuss.*, 2016, 1-50, 10.5194/acp-2016-549, 2016.
- Diederich, M., Ryzhkov, A., Simmer, C., Zhang, P., and Trömel, S.: Use of Specific Attenuation for Rainfall Measurement at X-Band Radar Wavelengths. Part I: Radar Calibration and Partial Beam Blockage Estimation, *Journal of Hydrometeorology*, 16, 487-502, doi:10.1175/JHM-D-14-0066.1, 2015.
- 40 Dipankar, A., Stevens, B., Heinze, R., Moseley, C., Zängl, G., Giorgetta, M., and Brdar, S.: Large eddy simulation using the general circulation model ICON, *Journal of Advances in Modeling Earth Systems*, 7, 963-986, 10.1002/2015MS000431, 2015.
- 45 Düsing, S., Wehner, B., Baars, H., Henning, S., Ma, N., Müller, T., Poulain, L., Seifert, P., Siebert, H., Tuch, T., and Wiedensohler, A.: Helicopter-borne observations of the continental background aerosol in combination with remote sensing and ground-based measurement, *Atmos. Chem. Phys.*, in preparation., 2017.
- 50 Eder, F., Schmidt, M., Damian, T., Träumner, K., and Mauder, M.: Mesoscale Eddies Affect Near-Surface Turbulent Exchange: Evidence from Lidar and Tower Measurements, *Journal of Applied Meteorology and Climatology*, 54, 189-206, doi:10.1175/JAMC-D-14-0140.1, 2015.
- 55 Engelmann, R., Wandinger, U., Ansmann, A., Müller, D., Žeromskis, E., Althausen, D., and Wehner, B.: Lidar Observations of the Vertical Aerosol Flux in the Planetary Boundary Layer, *Journal of Atmospheric and Oceanic Technology*, 25, 1296-1306, doi:10.1175/2007JTECHA967.1, 2008.

- Engelmann, R., Kanitz, T., Baars, H., Heese, B., Althausen, D., Skupin, A., Wandinger, U., Komppula, M., Stachlewska, I. S., Amiridis, V., Marinou, E., Mattis, I., Linné, H., and Ansmann, A.: The automated multiwavelength Raman polarization and water-vapor lidar PollyXT: the neXT generation, *Atmos. Meas. Tech.*, 9, 1767-1784, 10.5194/amt-9-1767-2016, 2016.
- 5 Ewald, F., Kölling, T., Baumgartner, A., Zinner, T., and Mayer, B.: Design and characterization of specMACS, a multipurpose hyperspectral cloud and sky imager, *Atmos. Meas. Tech. Discuss.*, 2015, 9853-9925, 10.5194/amtd-8-9853-2015, 2015.
- 10 Foth, A., Baars, H., Di Girolamo, P., and Pospichal, B.: Water vapour profiles from Raman lidar automatically calibrated by microwave radiometer data during HOPE, *Atmos. Chem. Phys.*, 15, 7753-7763, 10.5194/acp-15-7753-2015, 2015.
- Foth, A., Baars, H., Di Girolamo, P., and Pospichal, B.: Continuous Time Series of Water Vapor Profiles from a Combination of Raman Lidar and Microwave Radiometer, *EPJ Web of Conferences*, 119, 05001-05001, 2016.
- 15 Frisch, S., Shupe, M., Djalalova, I., Feingold, G., and Poellot, M.: The Retrieval of Stratus Cloud Droplet Effective Radius with Cloud Radars, *Journal of Atmospheric and Oceanic Technology*, 19, 835-842, 10.1175/1520-0426(2002)019<0835:trosced>2.0.co;2, 2002.
- Gatt, P., Barr, K., and Margulis, M.: WindTracer - Evolution and Recent Measurement Results, in: *OSA Technical Digest (online), Imaging and Applied Optics 2015*, Arlington, Virginia, 2015, LT3D.2,
- 20 Gendt, G., Reigber, C., and Dick, G.: Near real-time water vapor estimation in a German GPS network—first results from the ground program of the HGF GASP project, *Physics and Chemistry of the Earth, Part A: Solid Earth and Geodesy*, 26, 413-416, [http://dx.doi.org/10.1016/S1464-1895\(01\)00075-8](http://dx.doi.org/10.1016/S1464-1895(01)00075-8), 2001.
- 25 Görsdorf, U., Lehmann, V., Bauer-Pfundstein, M., Peters, G., Vavriv, D., Vinogradov, V., and Volkov, V.: A 35-GHz Polarimetric Doppler Radar for Long-Term Observations of Cloud Parameters—Description of System and Data Processing, *Journal of Atmospheric and Oceanic Technology*, 32, 675-690, 10.1175/jtech-d-14-00066.1, 2015.
- Gottschall, J., and Courtney, M.: Verification test for three WindCube WLS7 LiDARs at the Høvsøre test site, *Danmarks Tekniske Universitet, Risø Nationallaboratoriet for Bæredygtig Energi*8755038190, 2010.
- 30 Grzeschik, M., Bauer, H.-S., Wulfmeyer, V., Engelbart, D., Wandinger, U., Mattis, I., Althausen, D., Engelmann, R., Tesche, M., and Riede, A.: Four-Dimensional Variational Data Analysis of Water Vapor Raman Lidar Data and Their Impact on Mesoscale Forecasts, *Journal of Atmospheric and Oceanic Technology*, 25, 1437-1453, 10.1175/2007jtech974.1, 2008.
- 35 Hammann, E., Behrendt, A., Le Mounier, F., and Wulfmeyer, V.: Temperature profiling of the atmospheric boundary layer with rotational Raman lidar during the HD(CP)² Observational Prototype Experiment, *Atmos. Chem. Phys.*, 15, 2867-2881, 10.5194/acp-15-2867-2015, 2015.
- 40 Hande, L. B., Engler, C., Hoose, C., and Tegen, I.: Parameterising Cloud Condensation Nuclei concentrations during HOPE, *Atmos. Chem. Phys. Discuss.*, 2016, 1-29, 10.5194/acp-2016-357, 2016.
- Heese, B., Flentje, H., Althausen, D., Ansmann, A., and Frey, S.: Ceilometer lidar comparison: backscatter coefficient retrieval and signal-to-noise ratio determination, *Atmos. Meas. Tech.*, 3, 1763-1770, 10.5194/amt-3-1763-2010, 2010.
- 45 Heinze, R., Mironov, D., and Raasch, S.: Second-moment budgets in cloud topped boundary layers: A large-eddy simulation study, *Journal of Advances in Modeling Earth Systems*, 7, 510-536, 10.1002/2014MS000376, 2015.
- Heinze, R., Moseley, C., Böske, L. N., Muppa, S., Maurer, V., Raasch, S., and Stevens, B.: Evaluation of large-eddy simulations forced with mesoscale model output for a multi-week period during a measurement campaign, *Atmos. Chem. Phys. Discuss.*, 2016, 1-37, 10.5194/acp-2016-498, 2016.
- 50 Heinze, R., Dipankar, A., Henken, C. C., Moseley, C., Sourdeval, O., Trömel, S., Xie, X., Adamidis, P., Ament, F., Baars, H., Barthlott, C., Behrendt, A., Blahak, U., Bley, S., Brdar, S., Brueck, M., Crewell, S., Deneke, H., Di Girolamo, P., Evaristo, R., Fischer, J., Frank, C., Friederichs, P., Göcke, T., Gorges, K., Hande, L., Hanke, M., Hansen, A., Hege, H.-C., Hoose, C., Jahns, T., Kalthoff, N., Klocke, D., Kneifel, S., Knippertz, P., Kuhn, A., van Laar, T., Macke, A., Maurer, V., Mayer, B., Meyer, C. I., Muppa, S. K., Neggers, R. A. J., Orlandi,
- 55

- E., Pantillon, F., Pospichal, B., Röber, N., Scheck, L., Seifert, A., Seifert, P., Senf, F., Siligam, P., Simmer, C., Steinke, S., Stevens, B., Wapler, K., Weniger, M., Wulfmeyer, V., Zängl, G., Zhang, D., and Quaas, J.: Large-eddy simulations over Germany using ICON: a comprehensive evaluation, *Quarterly Journal of the Royal Meteorological Society*, n/a-n/a, 10.1002/qj.2947, 2017.
- 5 Heus, T., van Heerwaarden, C. C., Jonker, H. J. J., Pier Siebesma, A., Axelsen, S., van den Dries, K., Geoffroy, O., Moene, A. F., Pino, D., de Roode, S. R., and Vilà-Guerau de Arellano, J.: Formulation of the Dutch Atmospheric Large-Eddy Simulation (DALES) and overview of its applications, *Geosci. Model Dev.*, 3, 415-444, 10.5194/gmd-3-415-2010, 2010.
- 10 Holben, B. N., Tanré, D., Smirnov, A., Eck, T. F., Slutsker, I., Abuhassan, N., Newcomb, W. W., Schafer, J. S., Chatenet, B., Lavenu, F., Kaufman, Y. J., Castle, J. V., Setzer, A., Markham, B., Clark, D., Frouin, R., Halthore, R., Karneli, A., O'Neill, N. T., Pietras, C., Pinker, R. T., Voss, K., and Zibordi, G.: An emerging ground-based aerosol climatology: Aerosol optical depth from AERONET, *Journal of Geophysical Research: Atmospheres*, 106, 12067-12097, 10.1029/2001JD900014, 2001.
- 15 Illingworth, A. J., Hogan, R. J., O'Connor, E. J., Bouniol, D., Delanoë, J., Pelon, J., Protat, A., Brooks, M. E., Gaussiat, N., Wilson, D. R., Donovan, D. P., Baltink, H. K., Zadelhoff, G.-J. v., Eastment, J. D., Goddard, J. W. F., Wrench, C. L., Haefelin, M., Krasnov, O. A., Russchenberg, H. W. J., Piriou, J.-M., Vinit, F., Seifert, A., Tompkins, A. M., and Willén, U.: Cloudnet, *Bulletin of the American Meteorological Society*, 88, 883-898, doi:10.1175/BAMS-88-6-883, 2007.
- 20 IPCC: Climate Change 2013: The Physical Science Basis. Contribution of Working Group I to the Fifth Assessment Report of the Intergovernmental Panel on Climate Change, Cambridge University Press, Cambridge, United Kingdom and New York, NY, USA, 1535 pp., 2013.
- Jäkel, E., Walter, J., and Wendisch, M.: Thermodynamic phase retrieval of convective clouds: impact of sensor viewing geometry and vertical distribution of cloud properties, *Atmos. Meas. Tech.*, 6, 539-547, 10.5194/amt-6-539-2013, 2013.
- 25 Jakob, C.: Accelerating Progress in Global Atmospheric Model Development through Improved Parameterizations: Challenges, Opportunities, and Strategies, *Bulletin of the American Meteorological Society*, 91, 869-875, doi:10.1175/2009BAMS2898.1, 2010.
- 30 Kalisch, J., and Macke, A.: Estimation of the total cloud cover with high temporal resolution and parametrization of short-term fluctuations of sea surface insolation, *Meteorologische Zeitschrift*, 17, 603-611, 10.1127/0941-2948/2008/0321, 2008.
- 35 Kalthoff, N., Fiebig-Wittmaack, M., Meißner, C., Kohler, M., Uriarte, M., Bischoff-Gauß, I., and Gonzales, E.: The energy balance, evapotranspiration and nocturnal dew deposition of an arid valley in the Andes, *Journal of Arid Environments*, 65, 420-443, <http://dx.doi.org/10.1016/j.jaridenv.2005.08.013>, 2006.
- Kalthoff, N., Adler, B., Wieser, A., Kohler, M., Träumner, K., Handwerker, J., Corsmeier, U., Khodayar, S., Lambert, D., Kopmann, A., Kunka, N., Dick, G., Ramatschi, M., Wickert, J., and Kottmeier, C.: KITcube - a mobile observation platform for convection studies deployed during HyMeX, *Meteorologische Zeitschrift*, 22, 633-647, 2013.
- 40 Krauss, L., Hauck, C., and Kottmeier, C.: Spatio-temporal soil moisture variability in Southwest Germany observed with a new monitoring network within the COPS domain, *Meteorologische Zeitschrift*, 19, 523-537, 2010.
- Lohmann, G. M., Monahan, A. H., and Heinemann, D.: Local short-term variability in solar irradiance, *Atmos. Chem. Phys.*, 16, 6365-6379, 10.5194/acp-16-6365-2016, 2016.
- 45 Löhnert, U., Schween, J. H., Acquistapace, C., Ebell, K., Maahn, M., Barrera-Verdejo, M., Hirsikko, A., Bohn, B., Knaps, A., O'Connor, E., Simmer, C., Wahner, A., and Crewell, S.: JOYCE: Jülich Observatory for Cloud Evolution, *Bulletin of the American Meteorological Society*, 96, 1157-1174, doi:10.1175/BAMS-D-14-00105.1, 2015.
- 50 Madhavan, B. L., Deneke, H., Witthuhn, J., and Macke, A.: Multiresolution analysis of the spatiotemporal variability in global radiation observed by a dense network of 99 pyranometers during the HOPE campaign, *Atmos. Chem. Phys. Discuss.*, 2016, 1-33 10.5194/acp-2016-694, 2016a.
- 55 Madhavan, B. L., Kalisch, J., and Macke, A.: Shortwave surface radiation network for observing small-scale cloud inhomogeneity fields, *Atmos. Meas. Tech.*, 9, 1153-1166, 10.5194/amt-9-1153-2016, 2016b.

- Mamouri, R. E., and Ansmann, A.: Potential of polarization lidar to provide profiles of CCN- and INP-relevant aerosol parameters, *Atmos. Chem. Phys.*, 16, 5905-5931, 10.5194/acp-16-5905-2016, 2016.
- 5 Maronga, B., Gryschka, M., Heinze, R., Hoffmann, F., Kanani-Sühring, F., Keck, M., Ketelsen, K., Letzel, M. O., Sühring, M., and Raasch, S.: The Parallelized Large-Eddy Simulation Model (PALM) version 4.0 for atmospheric and oceanic flows: model formulation, recent developments, and future perspectives, *Geosci. Model Dev.*, 8, 2515-2551, 10.5194/gmd-8-2515-2015, 2015.
- 10 Maurer, V., Kalthoff, N., Wieser, A., Kohler, M., Mauder, M., and Gantner, L.: Observed spatiotemporal variability of boundary-layer turbulence over flat, heterogeneous terrain, *Atmos. Chem. Phys.*, 16, 1377-1400, 10.5194/acp-16-1377-2016, 2016.
- 15 McArthur, L. J. B.: World Climate Research Program - Baseline Surface Radiation Network (BSRN). Operations Manual Version 2.1, WCRP-121, WMO/TD-No. 1274 http://bsrn.awi.de/fileadmin/user_upload/bsrn.awi.de/Publications/McArthur.pdf, 2005.
- Merk, D., Deneke, H., Pospichal, B., and Seifert, P.: Investigation of the adiabatic assumption for estimating cloud micro- and macrophysical properties from satellite and ground observations, *Atmos. Chem. Phys.*, 16, 933-952, 10.5194/acp-16-933-2016, 2016.
- 20 Milovac, J., Branch, O.-L., Bauer, H.-S., Schwitalla, T., Warrach-Sagi, K., and Wulfmeyer, V.: High-Resolution WRF Model Simulations of Critical Land Surface-Atmosphere Interactions Within Arid and Temperate Climates (WRFCLIM), in: High Performance Computing in Science and Engineering '15: Transactions of the High Performance Computing Center, Stuttgart (HLRS) 2015, edited by: Nagel, E. W., Kröner, H. D., and Resch, M. M., Springer International Publishing, Cham, 607-622, 2016.
- Mülmenstädt, J., Sourdeval, O., Delanoë, J., and Quaas, J.: Frequency of occurrence of rain from liquid-, mixed-, and ice-phase clouds derived from A-Train satellite retrievals, *Geophysical Research Letters*, 42, 6502-6509, 10.1002/2015GL064604, 2015.
- 25 Muppa, S. K., Behrendt, A., Späth, F., Wulfmeyer, V., Metzendorf, S., and Riede, A.: Turbulent Humidity Fluctuations in the Convective Boundary Layer: Case Studies Using Water Vapour Differential Absorption Lidar Measurements, *Boundary-Layer Meteorology*, 158, 43-66, 10.1007/s10546-015-0078-9, 2016.
- 30 Myagkov, A., Seifert, P., Wandinger, U., Bühl, J., and Engelmann, R.: Relationship between temperature and apparent shape of pristine ice crystals derived from polarimetric cloud radar observations during the ACCEPT campaign, *Atmos. Meas. Tech.*, 9, 3739-3754, 10.5194/amt-9-3739-2016, 2016.
- Pearson, G., Davies, F., and Collier, C.: An Analysis of the Performance of the UFAM Pulsed Doppler Lidar for Observing the Boundary Layer, *Journal of Atmospheric and Oceanic Technology*, 26, 240-250, doi:10.1175/2008JTECHA1128.1, 2009.
- 35 Radlach, M., Behrendt, A., and Wulfmeyer, V.: Scanning rotational Raman lidar at 355 nm for the measurement of tropospheric temperature fields, *Atmos. Chem. Phys.*, 8, 159-169, 10.5194/acp-8-159-2008, 2008.
- 40 Rose, T., Crewell, S., Löhnert, U., and Simmer, C.: A network suitable microwave radiometer for operational monitoring of the cloudy atmosphere, *Atmospheric Research*, 75, 183-200, <http://dx.doi.org/10.1016/j.atmosres.2004.12.005>, 2005.
- Saeed, U., Rocadenbosch, F., and Crewell, S.: Adaptive Estimation of the Stable Boundary Layer Height Using Combined Lidar and Microwave Radiometer Observations, *IEEE Transactions on Geoscience and Remote Sensing*, PP, 1-12, 10.1109/TGRS.2016.2586298, 2016.
- 45 Schemann, V., and Seifert, A.: A Budget Analysis of the Variances of Temperature and Moisture in Precipitating Shallow Cumulus Convection, *Boundary-Layer Meteorology*, 1-17, 10.1007/s10546-016-0230-1, 2017.
- 50 Schmidt, T., Kalisch, J., Lorenz, E., and Heinemann, D.: Evaluating the spatio-temporal performance of sky-imager-based solar irradiance analysis and forecasts, *Atmos. Chem. Phys.*, 16, 3399-3412, 10.5194/acp-16-3399-2016, 2016.
- Schröder, M., Bennartz, R., Fischer, J., and Ruhtz, T.: Airborne remote sensing of cloud radiative smoothing during the Baltex Bridge Cloud campaign, *Atmospheric Research*, 72, 107-127, <http://dx.doi.org/10.1016/j.atmosres.2004.03.011>, 2004.
- 55 Schween, J. H., Hirsikko, A., Löhnert, U., and Crewell, S.: Mixing-layer height retrieval with ceilometer and Doppler lidar: from case studies to long-term assessment, *Atmos. Meas. Tech.*, 7, 3685-3704, 10.5194/amt-7-3685-2014, 2014.

- Seifert, P., Siebert, H., Bühl, J., Baars, H., Ebell, K., Preißler, J., Wehner, B., and Düsing, S.: Dynamical and microphysical properties of a stratocumulus cloud layer observed in-situ and with ground-based remote sensing, *Atmos. Chem. Phys.*, in preparation, 2017.
- 5 Siebert, H., Beals, M., Bethke, J., Bierwirth, E., Conrath, T., Dieckmann, K., Ditas, F., Ehrlich, A., Farrell, D., Hartmann, S., Izaguirre, M. A., Katzwinkel, J., Nuijens, L., Roberts, G., Schäfer, M., Shaw, R. A., Schmeissner, T., Serikov, I., Stevens, B., Stratmann, F., Wehner, B., Wendisch, M., Werner, F., and Wex, H.: The fine-scale structure of the trade wind cumuli over Barbados – an introduction to the CARRIBA project, *Atmos. Chem. Phys.*, 13, 10061-10077, 10.5194/acp-13-10061-2013, 2013.
- 10 Simmer, C., Thiele-Eich, I., Masbou, M., Amelung, W., Bogena, H., Crewell, S., Dieckrüger, B., Ewert, F., Franssen, H.-J. H., Huisman, J. A., Kemna, A., Klitzsch, N., Kollet, S., Langensiepen, M., Löhnert, U., Rahman, A. S. M. M., Rascher, U., Schneider, K., Schween, J., Shao, Y., Shrestha, P., Stiebler, M., Sulis, M., Vanderborght, J., Vereecken, H., Kruk, J. v. d., Waldhoff, G., and Zerenner, T.: Monitoring and Modeling the Terrestrial System from Pores to Catchments: The Transregional Collaborative Research Center on Patterns in the Soil–Vegetation–Atmosphere System, *Bulletin of the American Meteorological Society*, 96, 1765-1787, doi:10.1175/BAMS-D-13-00134.1, 15 2015.
- Skamarock, W. C., Klemp, J. B., Dudhia, J., Gill, D. O., Barker, D., Duda, M. G., Huang, X.-Y., Wang, W., and Powers, J. G.: A description of the advanced research WRF version 3, NCAR Technical Note, NCAR/TN-475+STR, 10.5065/D68S4MVH, 2008.
- 20 Späth, F., Behrendt, A., Muppa, S. K., Metzendorf, S., Riede, A., and Wulfmeyer, V.: 3-D water vapor field in the atmospheric boundary layer observed with scanning differential absorption lidar, *Atmos. Meas. Tech.*, 9, 1701-1720, 10.5194/amt-9-1701-2016, 2016.
- Spindler, G., Gnauk, T., Grüner, A., Inuma, Y., Müller, K., Scheinhardt, S., and Herrmann, H.: Size-segregated characterization of PM10 at the EMEP site Melpitz (Germany) using a five-stage impactor: a six year study, *Journal of Atmospheric Chemistry*, 69, 127-157, 25 10.1007/s10874-012-9233-6, 2012.
- Stannas, E., Lammert, A., Winkelmann, V., and Lang, U.: The HD(CP)2 Data Archive for Atmospheric Measurement Data, *ISPRS International Journal of Geo-Information*, 5, 10.3390/ijgi5070124, 2016.
- 30 Steinke, S., Eikenberg, S., Löhnert, U., Dick, G., Klocke, D., Di Girolamo, P., and Crewell, S.: Assessment of small-scale integrated water vapour variability during HOPE, *Atmos. Chem. Phys.*, 15, 2675-2692, 10.5194/acp-15-2675-2015, 2015.
- Stevens, B., and Lenschow, D. H.: Observations, Experiments, and Large Eddy Simulation, *Bulletin of the American Meteorological Society*, 82, 283-294, doi:10.1175/1520-0477(2001)082<0283:OEALES>2.3.CO;2, 2001.
- 35 Stevens, B., Moeng, C.-H., Ackerman, A. S., Bretherton, C. S., Chlond, A., Roode, S. d., Edwards, J., Golaz, J.-C., Jiang, H., Khairoutdinov, M., Kirkpatrick, M. P., Lewellen, D. C., Lock, A., Müller, F., Stevens, D. E., Whelan, E., and Zhu, P.: Evaluation of Large-Eddy Simulations via Observations of Nocturnal Marine Stratocumulus, *Monthly Weather Review*, 133, 1443-1462, 10.1175/mwr2930.1, 2005.
- 40 Tokay, A., Wolff, D. B., and Petersen, W. A.: Evaluation of the New Version of the Laser-Optical Disdrometer, OTT Parsivel2, *Journal of Atmospheric and Oceanic Technology*, 31, 1276-1288, doi:10.1175/JTECH-D-13-00174.1, 2014.
- Tørseth, K., Aas, W., Breivik, K., Fjæraa, A. M., Fiebig, M., Hjellbrekke, A. G., Lund Myhre, C., Solberg, S., and Yttri, K. E.: Introduction to the European Monitoring and Evaluation Programme (EMEP) and observed atmospheric composition change during 1972–2009, 45 *Atmos. Chem. Phys.*, 12, 5447-5481, 10.5194/acp-12-5447-2012, 2012.
- Träumner, K., Damian, T., Stawiarski, C., and Wieser, A.: Turbulent Structures and Coherence in the Atmospheric Surface Layer, *Boundary-Layer Meteorology*, 154, 1-25, 10.1007/s10546-014-9967-6, 2015.
- 50 Trömel, S., and Simmer, C.: An object-based approach for areal rainfall estimation and validation of atmospheric models, *Meteorology and Atmospheric Physics*, 115, 139-151, 10.1007/s00703-011-0173-5, 2012.
- Van Weverberg, K., Boutle, I. A., Morcrette, C. J., and Newsom, R. K.: Towards retrieving critical relative humidity from ground-based remote-sensing observations, *Quarterly Journal of the Royal Meteorological Society*, 142, 2867-2881, 10.1002/qj.2874, 2016.
- 55

- Wagner, G., Behrendt, A., Wulfmeyer, V., Späth, F., and Schiller, M.: High-power Ti:sapphire laser at 820 nm for scanning ground-based water-vapor differential absorption lidar, *Appl. Opt.*, 52, 2454-2469, 10.1364/AO.52.002454, 2013.
- 5 Wandinger, U., Freudenthaler, V., Baars, H., Amodeo, A., Engelmann, R., Mattis, I., Groß, S., Pappalardo, G., Giunta, A., D'Amico, G., Chaikovsky, A., Osipenko, F., Slesar, A., Nicolae, D., Belegante, L., Talianu, C., Serikov, I., Linné, H., Jansen, F., Apituley, A., Wilson, K. M., de Graaf, M., Trickl, T., Giehl, H., Adam, M., Comerón, A., Muñoz-Porcar, C., Rocadenbosch, F., Sicard, M., Tomás, S., Lange, D., Kumar, D., Pujadas, M., Molero, F., Fernández, A. J., Alados-Arboledas, L., Bravo-Aranda, J. A., Navas-Guzmán, F., Guerrero-Rascado, J. L., Granados-Muñoz, M. J., Preißler, J., Wagner, F., Gausa, M., Grigorov, I., Stoyanov, D., Iarlori, M., Rizi, V., Spinelli, N., Boselli, A., Wang, X., Lo Feudo, T., Perrone, M. R., De Tomasi, F., and Burlizzi, P.: EARLINET instrument intercomparison campaigns: overview on strategy and results, *Atmos. Meas. Tech.*, 9, 1001-1023, 10.5194/amt-9-1001-2016, 2016.
- 10 Wehner, B., Siebert, H., Hermann, M., Ditas, F., and Wiedensohler, A.: Characterisation of a new Fast CPC and its application for atmospheric particle measurements, *Atmos. Meas. Tech.*, 4, 823-833, 10.5194/amt-4-823-2011, 2011.
- 15 Wilson, A. M., and Jetz, W.: Remotely Sensed High-Resolution Global Cloud Dynamics for Predicting Ecosystem and Biodiversity Distributions, *PLOS Biology*, 14, e1002415, 10.1371/journal.pbio.1002415, 2016.
- Witthuhn, J., Deneke, H., Macke, A., and Bernhard, G.: Ship borne rotating shadow band radiometer observations for the determination of multi spectral irradiance components and direct sun products for aerosol, *Atmos. Meas. Tech. Discuss.*, 2016, 1-36, 10.5194/amt-2016-297, 2016.
- 20 Wulfmeyer, V., Pal, S., Turner, D. D., and Wagner, E.: Can Water Vapour Raman Lidar Resolve Profiles of Turbulent Variables in the Convective Boundary Layer?, *Boundary-Layer Meteorology*, 136, 253-284, 10.1007/s10546-010-9494-z, 2010.
- 25 Wulfmeyer, V., Behrendt, A., Kottmeier, C., Corsmeier, U., Barthlott, C., Craig, G. C., Hagen, M., Althausen, D., Aoshima, F., Arpagaus, M., Bauer, H.-S., Bennett, L., Blyth, A., Brandau, C., Champollion, C., Crewell, S., Dick, G., Di Girolamo, P., Dorninger, M., Dufournet, Y., Eigenmann, R., Engelmann, R., Flamant, C., Foken, T., Gorgas, T., Grzeschik, M., Handwerker, J., Hauck, C., Höller, H., Junkermann, W., Kalthoff, N., Kiemle, C., Klink, S., König, M., Krauss, L., Long, C. N., Madonna, F., Mobbs, S., Neininger, B., Pal, S., Peters, G., Pigeon, G., Richard, E., Rotach, M. W., Russchenberg, H., Schwitalla, T., Smith, V., Steinacker, R., Trentmann, J., Turner, D. D., van Baelen, J., Vogt, S., Volkert, H., Weckwerth, T., Wernli, H., Wieser, A., and Wirth, M.: The Convective and Orographically-induced Precipitation Study (COPS): the scientific strategy, the field phase, and research highlights, *Quarterly Journal of the Royal Meteorological Society*, 137, 3-30, 10.1002/qj.752, 2011.
- 30 Wulfmeyer, V., Hardesty, R. M., Turner, D. D., Behrendt, A., Cadeddu, M. P., Di Girolamo, P., Schlüssel, P., Van Baelen, J., and Zus, F.: A review of the remote sensing of lower tropospheric thermodynamic profiles and its indispensable role for the understanding and the simulation of water and energy cycles, *Reviews of Geophysics*, 53, 819-895, 10.1002/2014RG000476, 2015.
- 35 Wulfmeyer, V., Muppa, S. K., Behrendt, A., Hammann, E., Späth, F., Sorbjan, Z., Turner, D. D., and Hardesty, R. M.: Determination of Convective Boundary Layer Entrainment Fluxes, Dissipation Rates, and the Molecular Destruction of Variances: Theoretical Description and a Strategy for Its Confirmation with a Novel Lidar System Synergy, *Journal of the Atmospheric Sciences*, 73, 667-692, doi:10.1175/JAS-D-14-0392.1, 2016.
- 40 Wyngaard, J. C.: Toward Numerical Modeling in the "Terra Incognita", *Journal of the Atmospheric Sciences*, 61, 1816-1826, doi:10.1175/1520-0469(2004)061<1816:TNMITT>2.0.CO;2, 2004.
- 45 Xie, X., Evaristo, R., Simmer, C., Handwerker, J., and Trömel, S.: Precipitation and microphysical processes observed by three polarimetric X-band radars and ground-based instrumentation during HOPE, *Atmos. Chem. Phys.*, 16, 7105-7116, 10.5194/acp-16-7105-2016, 2016.
- 50 Zacharias, S., Bogen, H., Samaniego, L., Mauder, M., Fuß, R., Pütz, T., Frenzel, M., Schwank, M., Baessler, C., Butterbach-Bahl, K., Bens, O., Borg, E., Brauer, A., Dietrich, P., Hajnsek, I., Helle, G., Kiese, R., Kunstmann, H., Klotz, S., Munch, J. C., Papen, H., Priesack, E., Schmid, H. P., Steinbrecher, R., Rosenbaum, U., Teutsch, G., and Vereecken, H.: A Network of Terrestrial Environmental Observatories in Germany All rights reserved. No part of this periodical may be reproduced or transmitted in any form or by any means, electronic or mechanical, including photocopying, recording, or any information storage and retrieval system, without permission in writing from the publisher, *Vadose Zone Journal*, 10, 955-973, 10.2136/vzj2010.0139, 2011.
- 55

Zängl, G., Reinert, D., Ripodas, P., and Baldauf, M.: The ICON (ICOsahedral Non-hydrostatic) modelling framework of DWD and MPI-M: Description of the non-hydrostatic dynamical core, *Quarterly Journal of the Royal Meteorological Society*, 141, 563-579, 10.1002/qj.2378, 2015.

5

Figures and Tables

Table 1: Sites and networks deployed during HOPE-Jülich. Information on the individual instruments are given in Table 2. For details on the affiliations see Sec. 2.1.1. as well as the title page of this article.

Supersite or network	Abbreviation	Location	Instruments
Krauthausen	KRA	50.8797° N, 6.4145° E, 99 m asl	TROPOS: LACROS supersite with Mira-35, Polly ^{XT} , CHM15kx, WiLi, HATPRO, Parsivel2, Pyranometer, all-sky imager MPIM: Cimel
Jülich	JUE	50.909° N, 6.4139° E, 111 m asl	IGMK/FZJ: JOYCE with Mira-35, CHM15k, HALO Streamline, HATPRO, Parsivel2, all-sky imager, Cimel MPIM: ARL-2 UniBas: BASIL TROPOS: Pyranometer
Hambach	HAM	50.897° N, 6.463° E, 114 m asl	KIT: KITCube with Mira-35, Wind-Tracer, HALO Streamline, CHM15k, HATPRO, radiosonde station, Parsivel2, energy balance stations (at HAM and WAS sites, see Fig. 1), wind mast IPM: DIAL, TRRL MPIM: Cimel
Pyranometer network	PYR	Area enclosed by 50.846° N, 6.379° E and 50.945° N, 6.485° E. All pyranometers operated by TROPOS.	
Sky imager network	SKY	KRA: 50.897° N, 6.463° E, 99 m asl JUE: two instruments within 500 m of 50.909° N, 6.4139° E, 111 m asl	
X-band radar network	XRD	KIT: KiXPol at 50.8566° N, 6.3799° E, 114 m asl MIUB: BoXPol at 50.7312° N, 7.071 24° E, 99.5 m asl FZJ: JuXPol at 50.932° N, 6.455° E, 300 m asl All Instruments operated by the individual institutions.	
Sun photometer network	SUN	Aachen: 50.777° N, 6.0606° E, 230 m asl KRA: 50.879° N, 6.4145° E, 99 m asl Hombroich: 51.151° N, 6.6436° E, 70 m asl HAM: 50.897° N, 6.4630° E, 114 m asl JUE: 50.909° N, 6.4139° E, 111 m asl All instruments, except for JUE, provided by NASA/GSFC and operated by MPIM.	

Table 2: Details of instruments deployed during HOPE-Jülich and (in part, see Sec. 2.1.2) during HOPE-Melpitz.

Instrument	type	reference	sites / networks	measured quantities	atmospheric parameters	resolution
Lidar remote sensing						
Polly ^{XT}	multiwavelength Raman polarization lidar	Engelmann et al. (2016)	KRA	backscattered signal from molecules and particles	particle backscatter coefficient and extinction coefficient; linear depolarization ratio; water vapour mixing ratio	30 m; 30 s
BASIL	multiwavelength Raman polarization lidar	Di Girolamo et al. (2009)	JUE	backscattered signal from molecules and particles	profiles of particle backscatter coefficient and extinction coefficient, linear depolarization ratio, water vapour mixing ratio, temperature	7.5 m; 10 s
ARL-2	multiwavelength Raman polarization lidar	Wandinger et al. (2016)	JUE	backscattered signal from molecules and particles	profiles of particle backscatter coefficient and extinction coefficient, linear depolarization ratio, water vapor mixing ratio, temperature	7.5 m; 10 s
DIAL	differential absorption lidar	(Späth et al., 2016; Wagner et al., 2013)	HAM	backscattered signal from molecules and particles	absolute humidity 3D fields, particle backscatter 3D fields at 820 nm	15 m; 1 s
TRRL	rotational Raman temperature lidar	(Hammann et al., 2015; Radlach et al., 2008)	HAM	backscattered signal from molecules and particles	3D fields of temperature, water vapour mixing ratio, particle backscatter coefficient at 355 nm, particle extinction coefficient at 355 nm	3.75 m, 10 s
CHM15k(x)	lidar ceilometer	Heese et al. (2010)	KRA, HAM, JUE	backscattered signal from molecules and particles	cloud boundaries	10-30 s; 15 m
WiLi	Doppler lidar	Engelmann et al. (2008)	KRA	Doppler-shift along line-of-sight	profiles of vertical air velocity and horizontal wind	1-2 s; 75 m
Streamline	Doppler lidar	Pearson et al. (2009)	HAM, JUE	Doppler-shift along line-of-sight	profiles of vertical air velocity and horizontal wind	1-2 s; 15 m
WindTracer	Doppler lidar	Gatt et al. (2015)	HAM	Doppler-shift along line-of-sight	Doppler-shift along line of sight, SNR, vertical air velocity, radial air velocity, profiles of horizontal and vertical wind velocity	0.1/1 s (radial / vertical); 25-70 m
Windcube	Doppler lidar	Gottschall and Courtney (2010)	HAM	Doppler-shift along line-of-sight	Doppler-shift along line of sight, SNR, vertical air velocity, radial air velocity, profiles of horizontal and vertical wind velocity	1.6 s; 25 m
Radar remote sensing						
Mira-35, Mira-36S	35/36-GHz cloud radar	Görsdorf et al. (2015)	KRA, HAM, JUE, JUE	Radar reflectivity, Doppler spectrum, linear depolarization ratio	cloud boundaries, cloud structure, contributes to cloud liquid water profiles	15-30 m; 1-30 s
X-band radar	10-GHz precipitation radar	(Borowska et al., 2011; Kalthoff et al., 2013)	XRD	reflectivity, differential reflectivity, diff. phase, Doppler vel. and width, correlation coeff.	horizontal precipitation and boundary layer wind field	1 min, 100 m
Passive remote sensing						
HATPRO	microwave radiometer	Rose et al. (2005)	KRA, HAM, JUE	Atmospheric brightness temperatures from 22 to 58 GHz	temperature and humidity profile; liquid water path	1 s, 100-1000 m
CIMEL CE318	Sun photometer	Holben et al. (2001)	SUN	sky radiances	aerosol optical depth and volume size distribution, integrated water vapour	15 min
All-sky imager / Mobotix S14	fisheye camera	(Beekmans et al., 2016; Kalisch and Macke, 2008)	SKY	full sky images	cloud morphology	15 s, 120 s (S14)

Table 2, continued.

Instrument	type	reference	sites / networks	measured quantities	atmospheric parameters	resolution
Ground-based and in-situ observations						
Parsivel2	optical disdrometer	Tokay et al. (2014)	Bonn, HAM, KRA	size and velocity distribution of hydrometeors	precipitation rate, rain drop size distribution	30 s (Bonn, KRA), 60 s (HAM)
DFM-09	radiosonde	Bock et al. (2016)	HAM	pressure, humidity, temperature, GPS position	atmospheric pressure, temperature, humidity, wind vector	1 s
Pyranometer		Madhavan et al. (2016b)	PYR	photodiode voltage, bimetal voltage	broadband solar and thermal downward radiation fluxes, temperature	1 km, 1 s
Surface meteorology	energy balance stations and masts	Kalthoff et al. (2013)	HAM, JUE	temperature, humidity, pressure, wind vector, precipitation rate, radiation	surface and soil latent and sensible heat flux	0.05 s (turbulent fields), 1 s (met. data), 30 min (fluxes)

Table 3: Summary of Intensive Observation Periods during HOPE-Jülich. Coloured lines denote "Golden Days".

IOP No.	Date	sky situation
1	April 13	broken convective clouds
2	April 14	low-cloud deck until noon, broken cirrus in the afternoon
3	April 15	convective clouds, precipitation
4	April 18	few PBL clouds, broken cirrus
5	April 20	clear
6	April 24	clear
7	April 25	PBL clouds
8	April 26	frontal clouds, precipitation
9	April 29	weak convection
10	May 2	high aerosol load, cumulus
11	May 4	clear
12	May 5	PBL clouds
13	May 18	scattered clouds
14	May 19	scattered clouds
15	May 24	PBL convection in cold air mass
16	May 25	convective clouds, warm-front and precipitation in the evening
17	May 27	scattered clouds
18	May 28	scattered clouds, complex scenario

Table 4: Summary of Intensive Observation Periods during HOPE-Melpitz. On these days a total of 15 hours of observations with ACTOS were performed. Cu: Cumulus; Sc: Stratocumulus. Coloured rows denote "Golden Days".

IOP No.	Date	Sky situation	Flight times (UTC)
19	September 13	Cu clouds	08:43-12:40
20	September 14	polluted air, clear skies, Cu	08:10-10:20; 11:56-14:10
21	September 17	clean air, Cu	08:22-10:38
22	September 21	Cu convection, drizzling Sc decoupled from PBL	11:07-13:11
23	September 22	Sc decoupled from PBL	08:46-10:53
24	September 27	Cu convection, very low PBL	08:00-10:00

Table 5: Days of HOPE for which runs of the ICON model are available.

Date	IOP	Weather conditions
20.04.13	IOP 5	Clear sky with only some cirrus clouds in the morning and late afternoon
24.04.13	IOP 6	Clear-sky day with only few cirrus clouds in the morning and afternoon
25.04.13	IOP 7	Cloudy morning (up to 4/8) until 10 UTC, only few clouds during noon, afterwards again increasing cumulus humilis cloudiness
26.04.13	IOP 8	Rapidly increasing cloudiness up to complete overcast situation until noon, several rain showers and light to medium rain, decreasing cloudiness in the late afternoon
02.05.13	IOP 10	Broken cumulus mediocris cloudiness, decreasing cloud cover during afternoon
05.05.13	IOP 12	Clear-sky conditions until 09 UTC, afterwards slightly increasing cumulus humilis cloudiness up to (2/8)
11.05.13	-	High cloud cover until noon with several rain showers, afterwards broken cloudiness
28.05.13	IOP 18	Clear sky conditions until midday (10 UTC) with only very few cirrus clouds, following low cumulus humilis clouds until 17 UTC, afterwards rapidly increasing cloudiness with rain starting in the evening

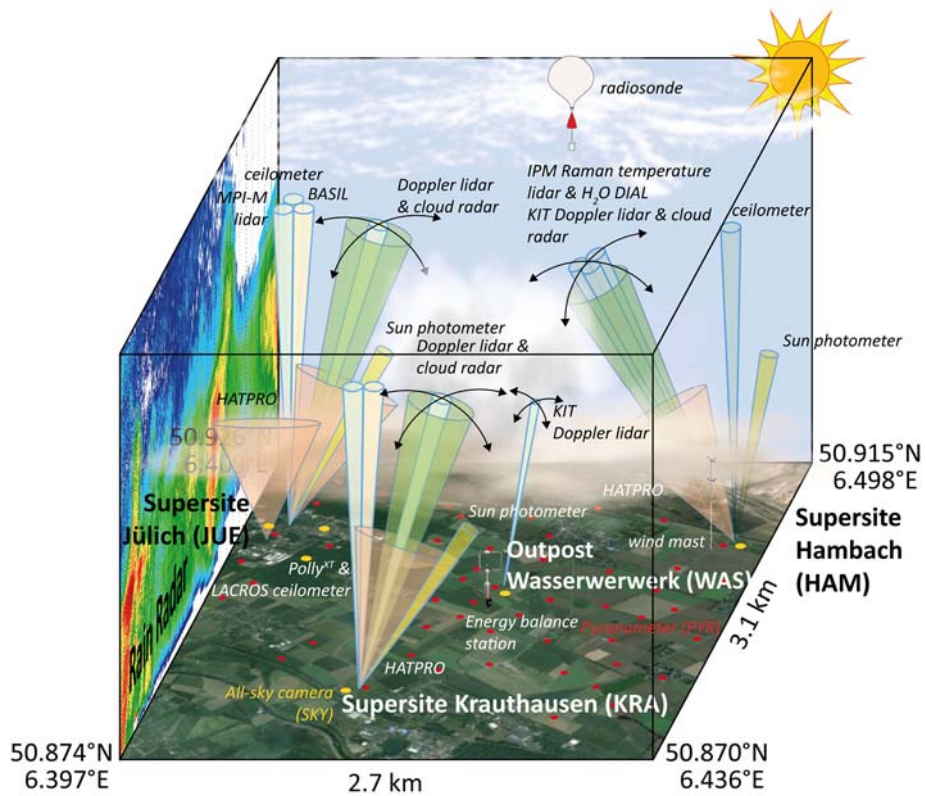


Figure 1: Setup of the HOPE-Jülich campaign showing the location of the three supersites Jülich (JUE), Hambach (HAM), and Krauthausen (KRA) as well as the outpost Wasserwerk (WAS) with their main instrumentation. The cones and arrows illustrate the field-of-view and scanning capabilities of the specific remote-sensing instruments.

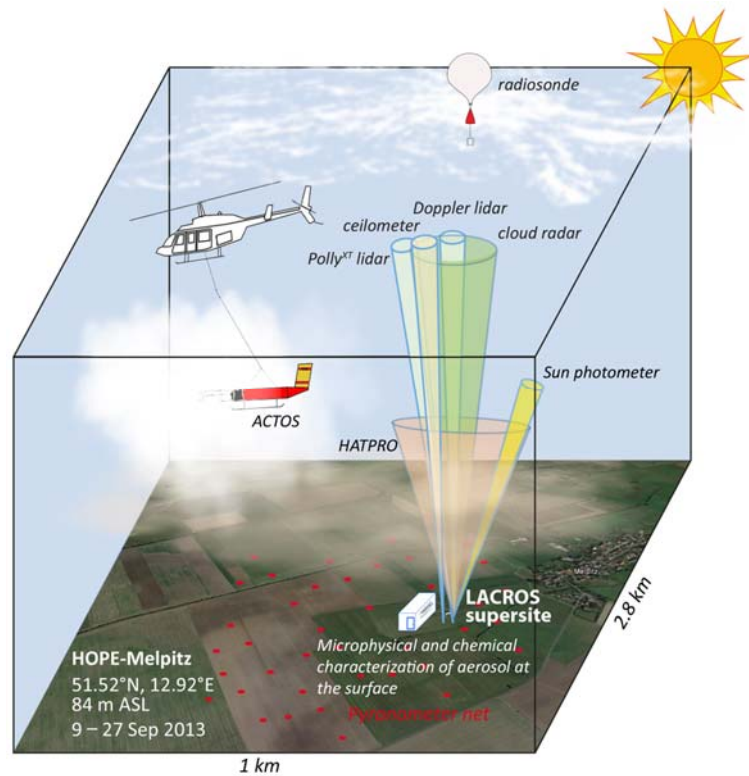


Figure 2: Illustration of the setup of the HOPE-Melpitz campaign showing the deployed main instrumentation. The cones illustrate the field-of-view of the specific remote-sensing instruments.

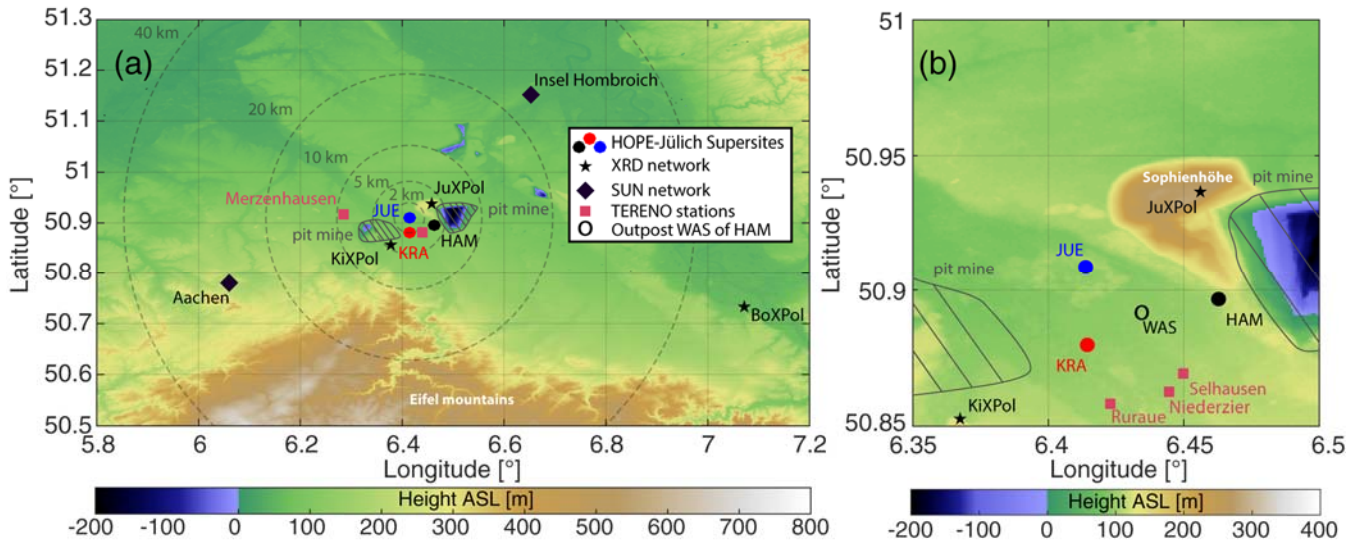


Figure 3: Map of the spatial distribution of the measurement sites and networks deployed according to Table 1 (left) and a zoomed-in view centred at supersite Jülich (right). Background colours indicate the topography and dashed lines denote circles of constant distance from supersite Jülich (JUE). Shaded areas denote open-pit mines, for which the elevation map is not up to date.

5

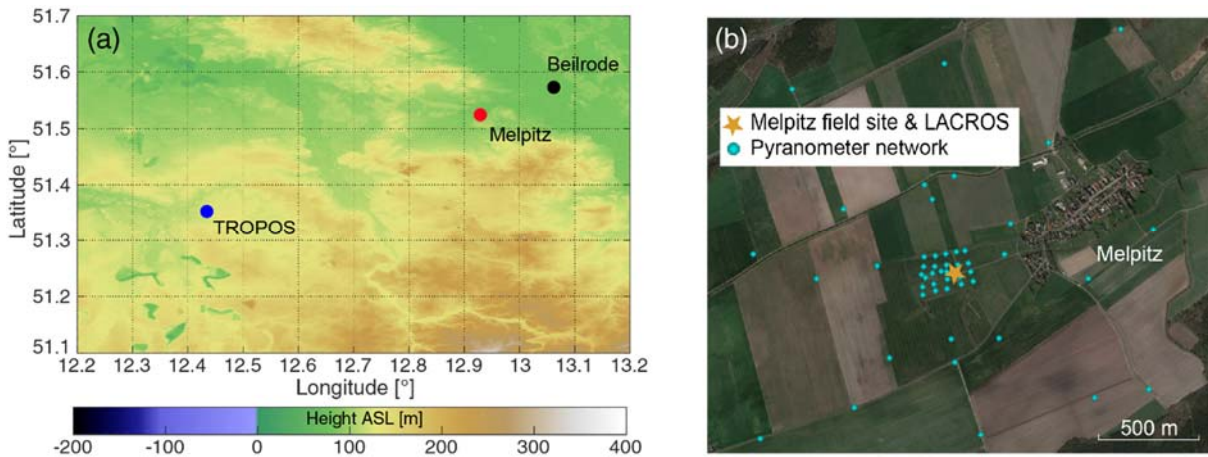


Figure 4: Topography around the location of the HOPE-Melpitz campaign. (a) large-scale topography; (b) aerial photograph of the Melpitz field site with the locations of the pyranometers of the PYR network.

10

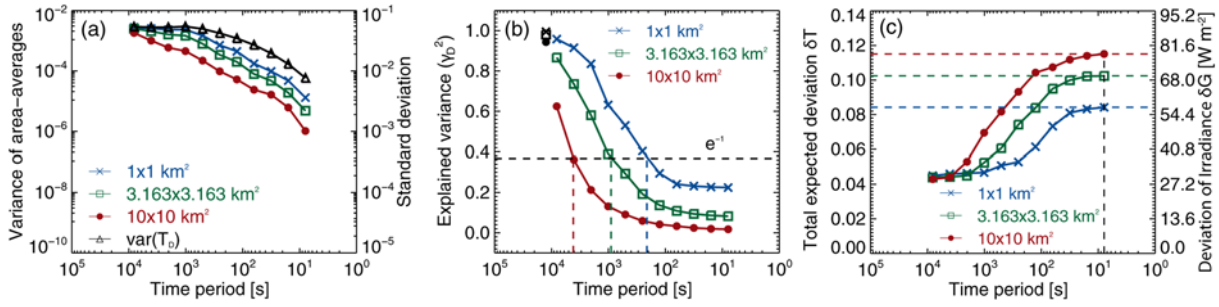


Figure 5: Spatiotemporal characteristics derived from the pyranometer network under broken-cloud conditions during HOPE-Jülich. This figure illustrates the origin of deviations between a point measurement (labelled as $\text{var}(T_0)$ in the legend) and a domain-averaged value (representativeness error) for broadband solar atmospheric transmittance and irradiance for different domain sizes. (a) Power spectra of transmittance for a point measurement and domains with different sizes; (b) Explained variance of temporal fluctuations in a point measurement and a domain average as function of period, and (c) total expected deviation between a point measurement and a domain average for transmittance and irradiance as a function of averaging, assuming a value of 680 W m^{-2} for the incoming solar irradiance at the top of atmosphere. The time period of fluctuations (inverse of their frequency) is shown logarithmically on the x-axis. Adapted from (Madhavan et al., 2016a).

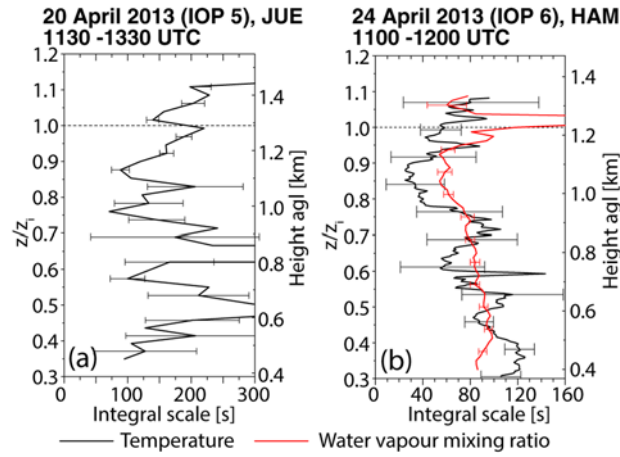


Figure 6: Integral scales of the temperature fluctuations (black) and humidity fluctuations (red) in the convective boundary layer derived from high-resolved temperature observations obtained between 1130 and 1330 on 20 April 2013 (IOP 5) and 1100 and 1200 UTC on 24 April 2013 (IOP 6) during HOPE-Jülich. Heights are normalized with respect to the height of the convective boundary layer height z_i . Adapted from Behrendt et al. (2015), Muppa et al. (2016), and from Di Girolamo et al. [2016].

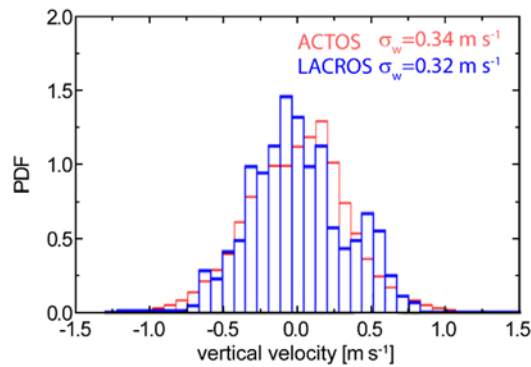


Figure 7: Simultaneous observation of the vertical velocity variations in a stratocumulus layer performed in-cloud with ACTOS (red) and at cloud base with Doppler lidar WiLi of LACROS (blue) on 22 September 2013 during HOPE-Melpitz. The mean vertical velocity of both observations was set to zero to correct for large-scale vertical motions. Adapted from Seifert et al. (2017).

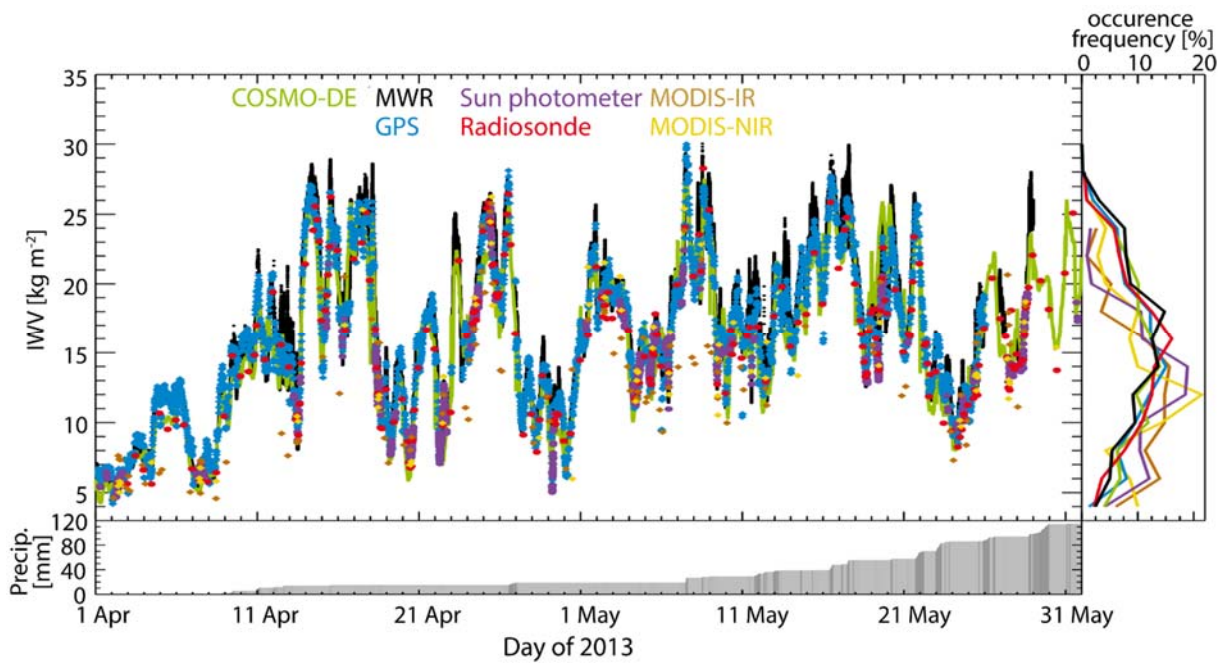


Figure 8: Observation of the integrated water vapour (IWV) during HOPE-Jülich for a large suite of different instruments. Right panel shows the frequency distribution of the IWV values recorded with the different techniques. Bottom panel shows the accumulated amount of precipitation. Adapted from Steinke et al. (2015).

5

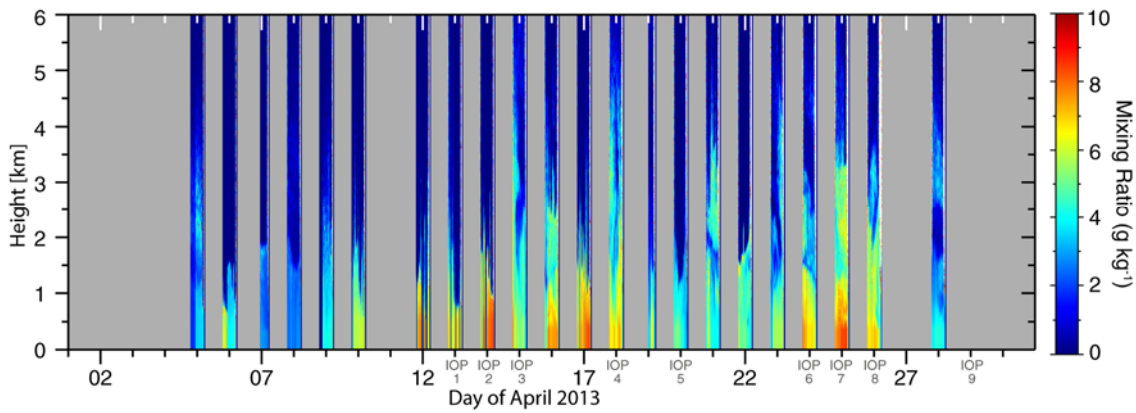


Figure 9: Calibrated nighttime observations at KRA of the water vapour mixing ratio for April 2013 during HOPE-Jülich obtained from Polly^{XT} that were calibrated automatically with the integrated water vapour provided by a co-located microwave radiometer. Adapted from Foth et al. (2015).

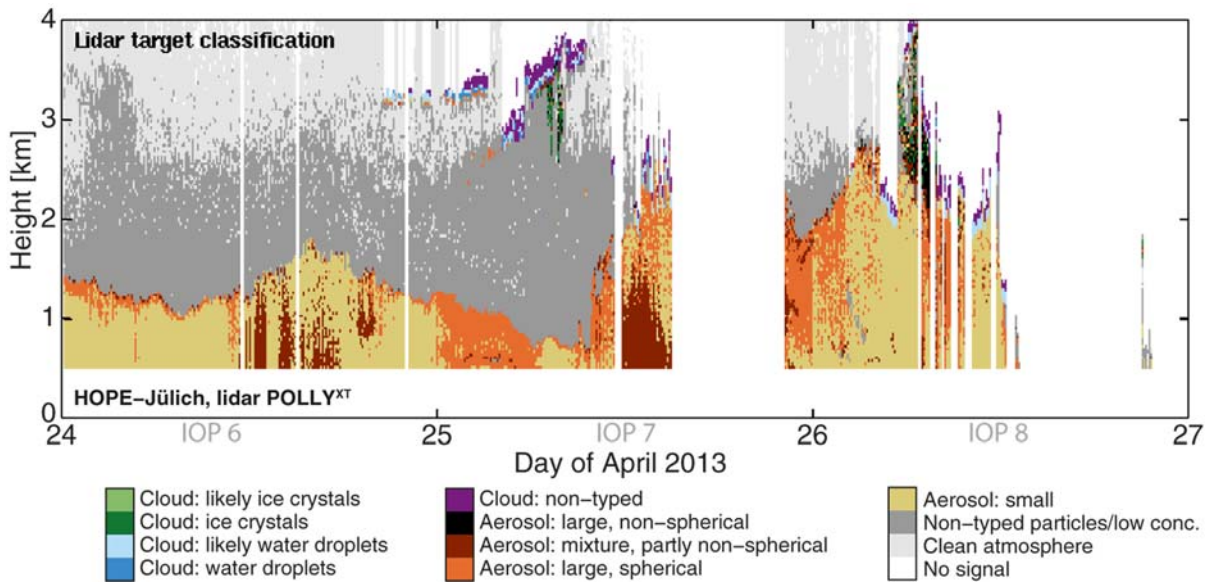


Figure 10: Aerosol target classification for the HOPE-Jülich period from 24 to 26 April 2013 (IOPs 6-8) based on continuous observations of the multi-wavelength polarization lidar Polly^{XT}. The methodology is described in Baars et al. (2017).

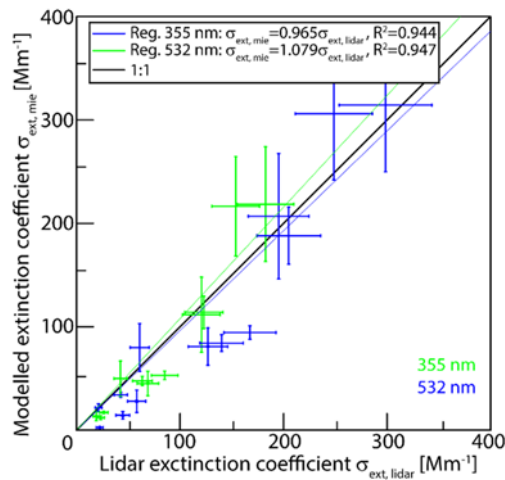


Figure 11: Correlation between the particle extinction coefficient derived from Mie modelling and hygroscopic-growth correction of in-situ measurements of ACTOS with the respective ones measured with Polly^{XT}. The data set is based on 13 data points obtained at different altitudes during two ACTOS flights on 14 and 17 September 2013 during HOPE-Melpitz. Adapted from Düsing et al. (2017).

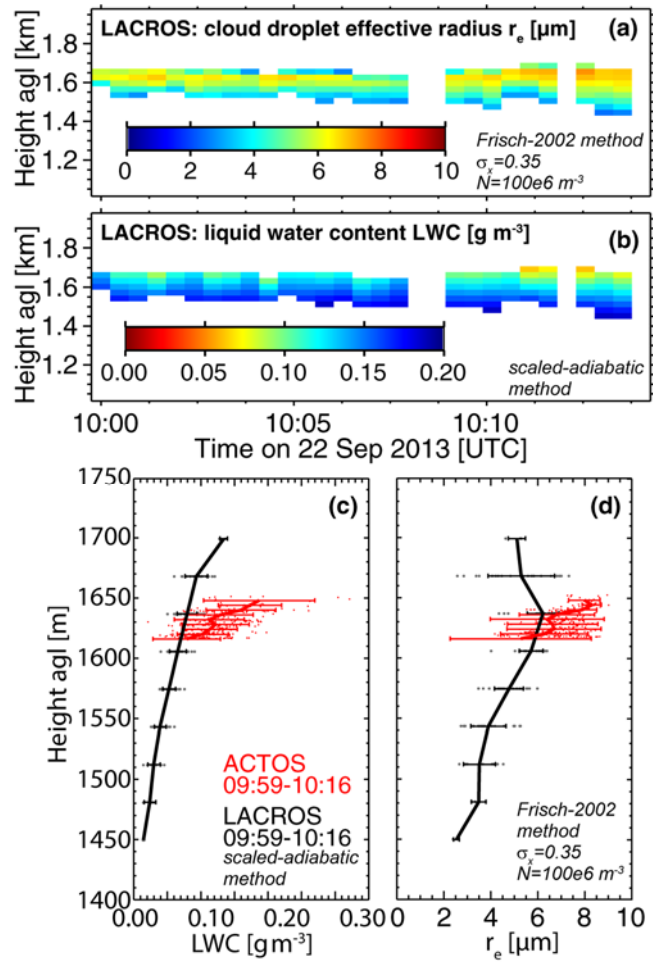


Figure 12: Stratocumulus observation at the Melpitz site on 22 September 2013. Time-height cross sections of (a) cloud droplet effective radius and (b) liquid water content as observed from ground-based remote sensing with LACROS. (c-d): Profiles of single data points, mean, and standard deviation (horizontal bars) of (c) liquid water content and (d) effective radius as observed in-situ with ACTOS (red) and retrieved from LACROS (black) for the time period shown in (a) and (b). Scaled-adiabatic method is based on Merk et al. (2016), Frisch-2002 method is based on Eq. 5 of Frisch et al. (2002).

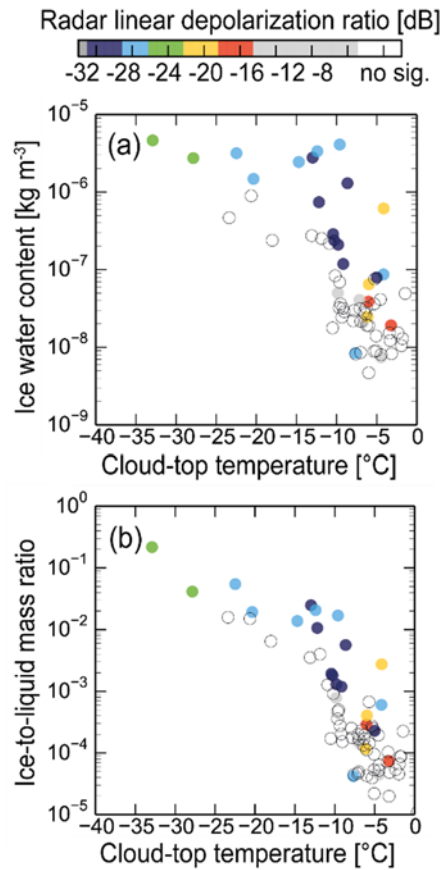


Figure 13: Relationship between mean ice water content (IWC) and ice-to-liquid mass ratio as a function of cloud top temperature of all thin supercooled stratiform clouds detected during HOPE-Jülich. The colours represent the different radar linear depolarization ratios.

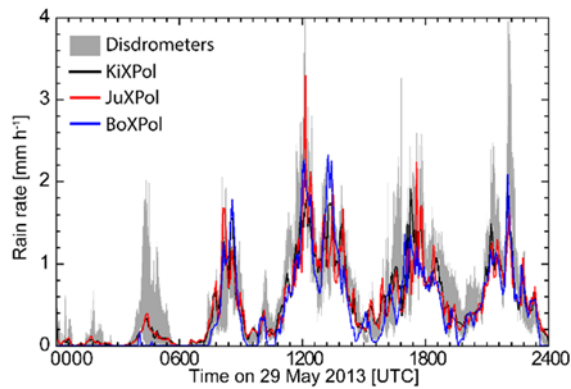


Figure 14: Time series of rain rates derived from observations of seven disdrometers (including those from the TR32 program) and the three polarimetric radars on 29 May 2013. The shaded grey area indicates the range of rain rates observed by the disdrometers with 1 min temporal resolution in the HOPE area, while the rain rate from the three polarimetric radar observations is calculated at the radar gates that are coincident with disdrometer locations and also averaged over the disdrometer locations. From Xie et al. (2016).

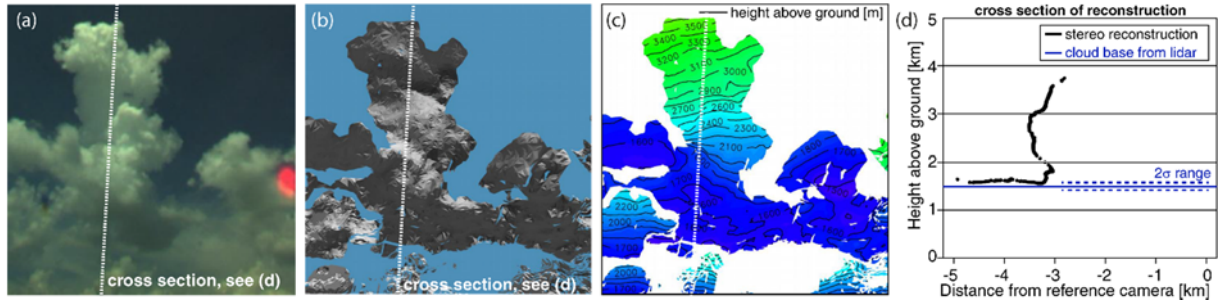


Figure 15: 3D reconstruction of a cumulus tower from a stereographic photograph from 24 July 2014, 11:32:00 UTC. Shown are (a) subsection of the image obtained from the reference camera, (b) the reconstruction as an untextured triangulated surface mesh, (c) the color-coded height of the reconstruction with contour lines, and (d) reconstructed distance of the cloud edges from the reference camera obtained along the cross-section (dashed line) shown in (a), (b), and (c) as well as a comparison of the cloud base with the one observed with lidar ceilometer (blue line). Adapted from Beekmans et al. (2016).

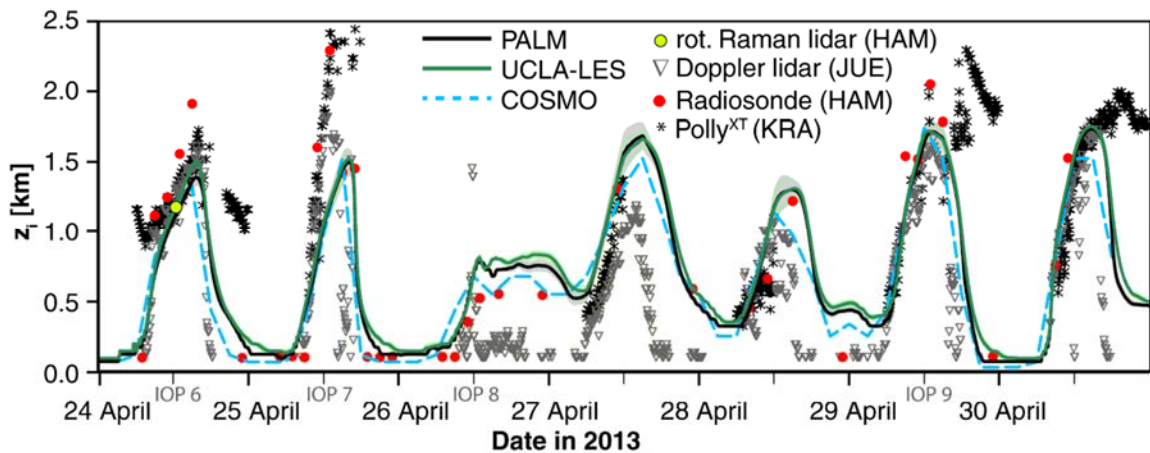


Figure 16: Temporal evolution of the boundary layer depth z_i for the period from 24 to 30 April 2013. z_i is determined by means of the bulk-Richardson number criterion in all three models (PALM, UCLA-LES and COSMO) and in the radiosonde data. A criterion based on the vertical velocity variance and detected aerosol layers is used for the wind lidar and aerosol lidar Polly^{XT}, respectively. The data point obtained from the temperature rotational Raman lidar (TRRL, rot. Raman lidar) is based on Behrendt et al. (2015). Radiosondes were launched at the KITcube site, the Doppler lidar and Polly^{XT} took measurements at sites JUE and KRA, respectively. Grey and green shading denote twice the standard deviation of z_i in PALM and UCLA-LES, respectively. Adapted from Heinze et al. (2016).